

Spring 2015

Electrospun Titanium Dioxide and Silicon Composite Nanofibers for Advanced Lithium Ion Batteries

Kathleen McCormac

Follow this and additional works at: <https://digitalcommons.georgiasouthern.edu/etd>

 Part of the [Materials Chemistry Commons](#)

Recommended Citation

McCormac, K., et al., Preparation of porous Si and TiO₂ nanofibres using a sulphur-templating method for lithium storage. 2015: p. 1-5. DOI: 10.1002/pssa.201431834.

This thesis (open access) is brought to you for free and open access by the Jack N. Averitt College of Graduate Studies at Georgia Southern Commons. It has been accepted for inclusion in Electronic Theses and Dissertations by an authorized administrator of Georgia Southern Commons. For more information, please contact digitalcommons@georgiasouthern.edu.

Electrospun Titanium Dioxide and Silicon Composite Nanofibers for Advanced Lithium Ion Batteries

by

Kathleen McCormac

(under the Direction of Ji Wu)

Abstract

A unique electrospinning method was implemented to fabricate composite nanofibers for lithium ion battery applications. The composite nanofibers were made of amorphous carbon, rutile phase TiO₂, and cubic phase Si nanoparticles. Sulfur was utilized as a template to form void structures within the TiO₂ nanofiber matrix. This provides the desired space for the Si expansion during the lithiation process. Phase, structure, composition, and morphology of the nanofibers were characterized using Raman spectroscopy, SEM, EDS, TGA, and powder XRD. Carbonized TiO₂ nanofibers showed a low but stable specific capacity. Si Nanoparticles demonstrated an initially high but fast degrading capacity. In contrast, silicon in SiNP/C/TiO₂ nanofibers with sulfur as a template exhibits an impressive high specific capacity of ~3459 mAh g⁻¹ initially, 54% of which can be maintained after 180 cycles.

Keywords: Lithium Ion Batteries, Titanium Dioxide, Silicon, Nanoparticles, High Capacity, Nanofiber, Sulfur Template

Electrospun Titanium Dioxide and Silicon Composite Nanofibers for Advanced Lithium Ion Batteries

by

Kathleen McCormac

B.S., Armstrong State University, 2013

A Thesis Submitted to the Graduate Faculty of Georgia Southern University in

Partial Fulfillment of the Requirements for the Degree of

MASTER OF SCIENCE

In

Applied Physical Sciences

Statesboro, Georgia

© 2015

Kathleen McCormac

All Rights Reserved

Electrospun Titanium Dioxide and Silicon Composite Nanofibers for Advanced Lithium Ion Batteries

by

Kathleen McCormac

Chairman: Ji Wu, chairman

Board Members: Rafael Quirino

John Stone

Electronic Version Approved:

May 2015

DEDICATION

To my friends for being there when I thought this would never be possible;

To my mentors for pushing me to think past what I know and brave the unknown;

To my parents for instilling hard work and drive in me for without you

this would never be possible.

ACKNOWLEDGEMENTS

I would like to acknowledge Georgia Southern University for the use of their facility. The Masters of Applied Physical Science program for their stipend and tuition assistance that has allowed me to attend and do research through the university. I would like to recognize the College of Science and Mathematics for their financial support through a graduate research grant to purchase supplies and the Georgia Southern Student Government Association for their financial support to travel to conferences. I would like to thank the chemistry department at Georgia Southern for their continued support of my research. I would like to acknowledge Dr. Ji Wu for his guidance as I progressed through the program. I would like to thank all the undergraduates who have helped me with these projects including Bryan Seymour, Ian Byrd, Rodney Brannen, and Stephen Trull. I would like to recognize the faculty and students at Georgia Southern including Dr. Hao Chen for his assistance with the SEM-EDS and TEM, Dr. McLemore for his assistance with the TGA, and Dr. Quirino along with his undergraduate research student Ashley Johns for their help with the Raman spectrometer. I acknowledge Dr. Cliff Padgett and Armstrong State University for the use and aid of their powder XRD.

Table of Contents

ACKNOWLEDGEMENTS	vi
List of Tables	ix
List of Figures	x
Chapter 1: Literature Review	1
1.1 Brief History of Batteries	1
1.2 Lithium Ion Batteries for energy storage and electric vehicles.....	2
1.3 How does a lithium ion battery function?	3
1.4 Ways to improve the electrochemical performance of Lithium Ion Batteries	4
1.4.1 Electrolyte	4
1.4.2 Membranes.....	7
1.4.3 Electrodes.....	8
1.5 Advantages and disadvantages of silicon in Lithium Ion Batteries	11
1.6 Nanoscale silicon for Lithium Ion Batteries	12
Chapter 2: Silicon Encapsulated in TiO ₂ Nanofibers.....	15
2.1 Introduction.....	15
2.2. Experimental	16
2.2.1 Chemicals.....	16
2.2.2 Instrumentation	17
2.2.3 Fabrication of Titanium Dioxide Nanofibers (TiO ₂ NF)	18
2.2.4 Fabrication of Silicon Nanoparticle (NP)/ Titanium Dioxide Nanofibers (SiNP/TiO ₂ NF and SiNP/C/TiO ₂ NF)	18
2.2.5 Fabrication of Silicon Nanoparticle/ Titanium DioxideNanofibers with Sulfur as a template (SiNP/TiO ₂ with S as a template and SiNP/C/TiO ₂ with S as a template).....	18
2.2.6 Electrospinning and Post-treatment	18
2.2.7. Battery Fabrication and Battery Test Conditions.....	19
2.3 Results and Discussion	20
2.3.1. Characterization	20
2.3.2. Electrochemical Performance	24
2.4. Summary	27
Chapter 3: Concluding Remarks	29
Figures	30

Tables.....	49
References.....	50
Addendum: (Silicon Micron Powder and Titanium Dioxide Composite Nanofibers for Lithium Ion Batteries).....	54
1. Experimental.....	54
1.1 Titanium Dioxide Nanofiber (TiO ₂).....	54
1.2 Silicon Micron Powder Titanium Dioxide (Si/TiO ₂) Nanofibers	54
1.3 Silicon/TiO ₂ Nanofiber with S as a template (Si/TiO ₂ with S as a template)	54
1.4 Electrospinning and Post-treatment	55
1.5 Electrode Preparation.....	55
1.6 Battery Fabrication.....	55
2. Characterization of Si micron powder nanofibers	56
3. Electrochemical Performance	57
4. Conclusion	57

List of Tables

Table 1: Surface Area of noncarbonized samples.....	49
Table 2: Surface Area of carbonized samples.....	49

List of Figures

Figure 1: Comparison of Lead-acid, alkaline, and lithium ion batteries' energy density of size versus weight.....	30
Figure 2: Lithiation and delithiation process of lithium ion batteries.....	30
Figure 3: Internal schematic for lithium ion batteries.....	31
Figure 4: Anode and cathode materials for advanced lithium ion battery.....	31
Figure 5: Molecular structure of the self-healing polymer.....	32
Figure 6: General schematic for the formation of void structure in SiNP/C/TiO ₂ NF with S as a template.....	32
Figure 7: General procedure for carbonized nanofibers.....	33
Figure 8: Fabrication method for processing nanofibers through sol-gel electrospinning: a) cartoon explanation and b) experimental set up.....	33
Figure 9: Scanning electron microscope images of a) carbonized SiNP, b) carbonized TiO ₂ NFs, c) carbonized SiNP/C/TiO ₂ NFs, d) noncarbonized SiNP/TiO ₂ NFs with sulfur as a template, and e) carbonized SiNP/C/TiO ₂ NFs with sulfur as the template.....	34
Figure 10: Histogram representation of the diameters of the carbonized TiO ₂ , SiNP/C/TiO ₂ , and SiNP/C/TiO ₂ with S template.....	35
Figure 11: a) Magnified SEM image and b) TEM image of carbonized SiNP/C/TiO ₂ NF with S as template.....	35
Figure 12: Powder XRD patterns for a) non-carbonized composite nanofibers and b) carbonized SiNP/C/TiO ₂ NF with S as a template.....	36
Figure 13: Raman Spectrum and characterization of the carbonized NFs.....	37
Figure 14: TGA data of carbonized a) TiO ₂ NF, b) SiNP, c) SiNP/C/TiO ₂ NF, d) SiNP/C/TiO ₂ with S template, and e) original pure SiNP	38
Figure 15: a) Cycling performance and b) coulombic efficiency of noncarbonized samples.....	42
Figure 16: Specific capacity of carbonized composite nanofibers.....	45
Figure 17: Voltage profile of carbonized composite nanofibers.....	46
Figure 18: Coulombic efficiency, overall specific capacity, and specific capacity of SiNP contribution of the carbonized SiNP/C/TiO ₂ NF with S as a template.....	47

Figure 19: C-rate performance of carbonized SiNP/C/TiO₂ NF with S as a template.....48

Chapter 1: Literature Review

Currently, non-renewable fossil fuels are dominating the global energy consumption; thus it makes us vulnerable to oil exporting nations and our economy unsustainable. In addition, the over usage of fossil fuels also increases the amount of CO₂ emissions into the atmosphere. The increased levels of CO₂ can lead to the acidification of the oceans, depletion of the Earth's ozone layer, and overall global warming [1]. This causes urgency and increases the importance of utilizing green energy resources like wind, hydroelectric, and solar power. However, the use of these intermittent power sources requires efficient energy storage devices. In this regard, batteries, especially lithium ion batteries, can play an important role. There are many types of batteries that affect our daily life, including but not limited to lead-acid batteries, alkaline batteries, and lithium-ion batteries.

1.1 Brief History of Batteries

Batteries were introduced during the Parthian era in Iraq [2]. They used lemon juice, grape juice, or vinegar as the electrolyte. Many years later, Luigi Galvani unexpectedly created the galvanized battery in 1789 [3]. The lead acid battery was invented by Gaston Planté in 1859. A lead-acid battery suitable for cars was not realized until Camille Faure in 1881 [2]. As seen in Figure 1, lead-acid batteries are very heavy, bulky, and have a low energy density (0.3 MJ L⁻¹) [4, 5]. Batteries produced using an alkaline electrolyte rather than acid were first developed by Waldemar Jungner in 1899. Thomas Edison, working independently from Jungner, was also able to create alkaline batteries in 1901 [2]. Rechargeable batteries like Ni-Cd or Ni-MH are lighter and smaller in size than the lead acid battery, but still have relatively small energy densities [5]. Ni-MH batteries have an energy density of 0.5 MJ L⁻¹ with a storage mass of 750 kg (Figure 1) [4].

While working at Exxon, M.S. Whittingham first proposed lithium batteries in the 1970s [2]. Lithium ion batteries (LIBs) are the most promising battery for their lighter weight, smaller size, and higher capacity [1]. LIBs have an energy density of 1.0 MJ L^{-1} with a lower storage mass than lead-acid or alkaline batteries (300kg) (Figure 1) [4]. Commercially available non-rechargeable lithium ion batteries are typically made of a transition metal oxide cathode and a lithium anode [6-9]. Companies such as the SONY Corporation and Panasonic have commercialized a $\text{Li}_{1-x}\text{CoO}_2/\text{C}$ rechargeable LIB to provide energy for mobile electronic devices like the camcorder and cell phone. However, the volumetric and gravimetric energy density of current rechargeable LIBs needs to be further increased as demanded by mobile electronics, electrical vehicles, and static intermittent power storage industries increases. Many research groups have carried out extensive studies to better the performance of LIBs including making them less harmful to the environment, lowering the fabrication cost, enhancing the safety, and increasing the capacity and cycling life.

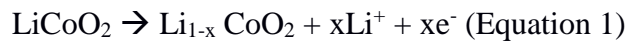
1.2 Lithium Ion Batteries for energy storage and electric vehicles

Lithium ion batteries are widely viewed as an optimal candidate for green energy storage and all-electric vehicles. They have also been extensively used in modern portable electronic devices [1, 10]. The storage of intermittent power sources like wind and solar energy requires efficient batteries [1]. The development of smaller and thinner electronics demands LIBs with higher operating cycles and a higher volumetric energy density [1, 9]. Additionally, hybrid and all-electric vehicles need LIBs with higher safety quality and energy density [9]. Theoretical energy densities required for all-electric vehicles are 10 MJ kg^{-1} of active electrode material [4]. Alloy electrodes such as tin and silicon possess theoretical capacities of 3.6 and 14.4 MC kg^{-1} ,

respectively, making them reasonable candidates for use as electrode materials in all-electric vehicles [4].

1.3 How does a lithium ion battery function?

To facilitate research on the optimization of lithium ion batteries, an understanding of the inner workings would significantly promote the research topic. Lithium ion batteries are powered by the transfer of lithium ions between anode and cathode host materials [1]. During the charging process, or lithiation, reduction occurs at the anode and oxidation occurs at the cathode. During the discharging process, or delithiation, oxidation occurs at the anode and reduction occurs at the cathode. The overall capacity of lithium ion battery is determined by the capacity of both anode and cathode materials, i.e. how much lithium ions these anode and cathode materials can store gravimetrically or volumetrically. Commercially available rechargeable lithium ion batteries are typically made of graphite anodes and cobalt oxide cathodes [6-9, 11]. At the positive electrode (cathode), the charging process equation is:



At the negative electrode (anode), the charging process is as follows:



[11]. The charging and discharging processes of LIBs are shown in Figure 2 [12]. It takes six carbon atoms of a graphite sheet to store one lithium ion (LiC_6). In contrast, one silicon atom can store 4.4 lithium atoms [7, 13]. As a result, the theoretical capacity of a commercial graphite anode is only 372 mAh g^{-1} , while silicon has an impressive theoretical capacity of 4200 mAh g^{-1} [7].

During the lithiation and delithiation processes, solid electrolyte interface (SEI) layers are formed on the surface of the electrodes. These layers stabilize the electrodes and help prevent the

leaching of materials into the electrolytes causing degradation of the battery. Irreversible capacity loss happens during the formation of these layers [14, 15]. SEI layers are mainly comprised of polyethylene glycol, lithium alkyl oxide, Li_2CO_3 , lithium alkyl carbonate, and other inorganic compounds, whose exact compositions can vary depending on the electrolytes, additives, and electrodes used [15].

1.4 Ways to improve the electrochemical performance of Lithium Ion Batteries

There are several ways to increase the capacity and stability of the LIBs. Each component of LIBs can be improved to create a better working battery as shown in Figure 3. The main components of the battery that can be manipulated are the anode, cathode, electrolyte, and membrane separator [1].

1.4.1 Electrolyte

Changing the electrolyte helps increase the diffusion ability between the anode and cathode. Different electrolytes are used for different materials as well as with different membranes. Electrolytes can be either liquid, gel, or solid [1]. Commercially available electrolytes for lithium ion batteries are 1M $\text{LiPF}_6/\text{EC}:\text{EMC}$ (ethylene carbonate: ethyl methyl carbonate) 1:3 with an ionic conductivity of 8.8 mS cm^{-1} and 1M $\text{LiPF}_6/\text{EC}:\text{DMC}:\text{DEC}:\text{EMC}$ (ethylene carbonate: dimethyl carbonate: diethyl carbonate: ethyl methyl carbonate) 1:1:1:3 with an ionic conductivity of 10 mS cm^{-1} [16]. Liquid electrolytes have the highest ionic conductivity ($>10^{-3} \text{ S cm}^{-1}$) for lithium ion batteries, then gel electrolytes ($>10^{-4} \text{ S cm}^{-1}$), finally solid electrolytes ($<10^{-4} \text{ S cm}^{-1}$) [17]. Liquid electrolytes for further improvement of LIB include organic liquid electrolytes such as LiClO_4 , LiPF_6 , and LiTFSI in different organic solvents such as carbonate esters: propylene carbonate (PC), ethylene carbonate (EC), ethyl methyl carbonate (EMC), and dimethyl carbonate (DMC) [17]. Ionic liquid electrolytes and aqueous liquid electrolytes are also options for batteries. Aqueous

liquid electrolytes are used in previous generation batteries such as alkaline batteries. These types of electrolytes are considered green electrolytes because they are typically water-based solution of a lithium salt [17]. Examples of this type of electrolyte are Li_2SO_4 and LiNO_3 . These electrolytes are also low in cost. Ionic liquid electrolytes are considered molten salts at room temperature [17]. This type of electrolyte helps improve the ionic conductivity. It enhances the performance and is of the greatest interest for energy storage applications [17]. The most common types of ionic liquid electrolytes for cation transition include N,N-diethyl-N-methyl-N-(2-methoxyethyl)ammonium, N-methyl-N-alkyl pyrrolidinium, and 1,2-alkyl methylimidazolium. While, the most common types of ionic electrolytes for anionic transition include bis(fluorosulfonyl)imide, bis(trifluoromethanesulfonyl)imide, hexafluorophosphate, and tetrafluoroborate [17]. Due to their relatively high price, ionic liquid electrolytes are not commercialized yet.

One research paper discussed that electrochemical performance of electrodes can be dramatically affected using different types of liquid electrolytes. Sn-O-C composite electrodes were fabricated into LIBs using LiPF_6 and LiClO_4 as electrolytes. The batteries which used LiPF_6 demonstrated a pulverization of the active electrode compared to that of LiClO_4 . The group concluded that this was due to the production of HF within the battery [18]. The specific capacity of the batteries was also drastically different. The LIB using LiPF_6 as the electrolyte only had a capacity of 69 mAh g^{-1} while the LIB using LiClO_4 had an impressive capacity of 473 mAh g^{-1} [18].

A review paper on the different types of solid electrolytes used in lithium ion batteries was studied for this examination. Poly (ethylene oxide) (PEO) is one of the earliest studied electrolytes. PEO is usually used between 40 and 100°C . PEO has an ionic conductivity of between 10^{-8} and 10^{-4} due to its high crystallinity [19, 20]. PEO can be doped with lithium salts to significantly

increase its ionic conductivity, such as PEO-LiCF₃SO₃ [19]. Most of this research focuses on lowering the glass transition (T_g) temperature or reducing the crystallinity of the polymer electrolytes [21]. This was done by using blends, copolymers, branch polymers, and cross-linked networks. Incorporating plasticizers into the polymer electrolytes has proved to be one of the most efficient ways to increase the ionic conductivity. Plasticizers allow for more efficient transportation of charges [21]. Another plasticizer group studied was poly (ethylene glycol) (PEG) with PEO-LiCF₃SO₃. It possesses the same repeating unit as PEO would with more amorphous regions, thus allowing for lower T_g . This, however, is not an excellent electrolyte because the end-groups (-OH) can react with lithium metal which can lead to a high initial capacity loss. In order to fix this problem, the hydroxyl end groups were replaced with mono- and di-methoxy complexes. Although this mixture was electrochemically stable, it had a much lower ionic conductivity [21].

Polyacrylonitrile (PAN) is another polymer used for solid electrolytes in lithium-ion batteries because it has the ability to maintain high conductivity at room temperature [21]. Homogenous hybrid films were created from PAN salt and a plasticizer mixture. The plasticizers that were used included ethylene carbonate, propylene carbonate, and N,N-dimethylformamide mixed with LiClO₄ in PAN. This created a solution that is suitable for lithium-ion batteries usage [21]. Intensive research is currently being done on PAN containing zeolite powders dispersed in PAN gels with LiAsF₆. This is beneficial in the fact that the zeolite increases the ionic conductivity at room temperature by affecting the crystallinity of the PAN and slows the growth of the resistive layer on the lithium surface [21]. The stability of the electrodes can be increased which is always beneficial in lithium ion batteries.

Poly (methyl methacrylate) (PMMA) is another type of polymer discussed in the review article for its use as an electrolyte in lithium-ion batteries. PMMA is also doped with lithium salts

to enhance its ionic conductivity. For example, PMMA electrolytes can be mixed with EC/PC-LiX where X can be ClO_4^- , AsF_6^- , or $[\text{N}(\text{CF}_3\text{SO}_2)_2]^-$. PMMA can be produced at high molecular weight. The high molecular weight “imparts a very high macroscopic viscosity to the system without significantly diminishing the conductivity” [21]. This high conductivity is very close to that of liquid electrolytes even in the gel form. This means that the PMMA does not impact the electrochemical stability, but allows for quick ion transport using the propylene carbonate. When PMMA is dissolved up to 20 wt. % in LiClO_4 (1 M)-PC electrolyte the ionic conductivity is $2.3 \times 10^{-3} \text{ S cm}^{-1}$.

Polyvinylidene fluoride (PVDF) was the final polymer discussed for its use as a polymer gel electrolyte. The fluorine atoms create a strong electron withdrawing group [21]. This allows the polymer to be highly stable. It also has a high dielectric constant unlike the other polymers studied. This implies that it has a greater ionization of lithium salts and provides the ability to carry more charges through the electrolyte. Li-doped PVDF has an ionic conductivity of $1.74 \times 10^{-3} \text{ Scm}^{-1}$. PVDF, like the other polymers, can be mixed with plasticizers to change its crystallinity and ionic conductivity. Noteworthy, low-molecular weight plasticizers can cause homogeneity in the polymer blend at low temperatures. This makes the fabrication process less controllable [21]. Also, direct connection between the PVDF and lithium metal creates LiF and degrades the electrode rendering it incompatible for use in lithium-ion batteries. However, through the use of new membranes PVDF has sparked new research initiatives in more recent years [21].

1.4.2 Membranes

Optimizing the membrane can be beneficial because it can facilitate a quicker charging or discharging process. Microporous membranes are prepared using phase inversion of polymer solutions [22]. It is important for the membranes to be porous thus allowing the transport of

electrolyte during the processes of lithiation and delithiation. In one study, a polyethylene membrane is coated with poly (vinylidene fluoride-co-hexafluoropropylene) (PVdF-HFP) dissolved in electrolyte of Li-PF₆ in a 1:1 w/w ethylene carbonate to diethyl carbonate [22]. This was used in a graphite anode/ lithium manganese oxide cathode battery. Coating membranes can prevent leaching from occurring in LIBs. The cycling performance shows that lithiation and delithiation occurs and is quite stable. The discharge capacity starts around 160 mAh g⁻¹ and only loses around 19% of its capacity after 200 cycles [22]. This however is still not as good as commercially available batteries. Another group experimented using PVdF-HFP dissolved in acetone [23]. This is very similar to that of the first experimental design. In this paper, the cycle performance was only stable for 47 cycles [23].

Another article used a different polymer for coating the membrane, Poly(acrylonitrile-co-methyl methacrylate-co-styrene) (PAMS) [20]. This polymer was coated onto a polyethylene membrane. This was done using a graphite anode and a LiCoO₂ cathode. The cycling performance of this type of battery was stable as well but had a lower capacity of ~75 mAh g⁻¹ to 70 mAh g⁻¹ for 50 cycles [20].

1.4.3 Electrodes

The anode and cathodes can be made of different materials whose theoretical capacities are shown in Figure 4. Initially, an all lithium metal battery was utilized because of its high capacity. However, when this type of LIB begins the cycle of charging and discharging dendrites are formed on the surface of the lithium electrodes. These dendrites can pierce through the membrane surface and shorten the cathode and anode. This creates overheating and explosion which is not safe for handlers [5]. Many different chemical additives have been researched to better the capacity without the creation of dendrites. Most cathode materials are transition metal oxides while most anode

materials are metals and metalloids. As seen in Figure 4, anode materials operate at a lower voltage while cathode materials operate at higher voltages. Also visible in this figure, is the dramatic increase in capacity from graphite of commercial lithium ion batteries to tin, germanium, and silicon [12].

Sulfur is a tricky chemical to use in batteries as a cathode material because it is an insulator. Soluble polysulfides are generated during the discharging process which can leach into the electrolyte and rapidly degrade the battery [24]. Most Li-S batteries must have a (C-rate) below 0.5C because of its low electrical conductivity [25].

C-rate is a term describing the rate of charging/discharging process. For 1C charging rate, it takes 1 hour to charge the battery to its full capacity. The higher the C-rate is, the quicker the ability to charge the battery to full capacity.

Choi and his collaborators used a two-step coating process where mesoporous carbon was first immersed in a solution of sulfur dispersed in carbon disulfide and then dried to evaporate the CS₂. Next, the sulfur-mesoporous carbon was annealed in nitrogen gas at 140°C for 1 hour. This stepwise fashion allowed the sulfur to be protected from leaching by trapping polysulfide within the carbon during the discharging process. This process allowed for the initial capacity to be increased to 1178 mAh g⁻¹; however, it degrades to 500 mAh g⁻¹ in 50 cycles [24]. This capacity is still much higher than that of commercially available cathodes which are commonly lower than 200 mAh g⁻¹.

Metals, metalloids, and their oxides are among the most favorable contenders for anode materials because of their high theoretical capacities [9]. Germanium has a theoretical capacity of 1384 mAh g⁻¹ [26]. This is shown in the delithiation equation for germanium:



Germanium nanowires have been studied for their impressive ability to have a long and stable cycle life at a high capacity. Kennedy from the University of Limerick and his collaborators were able to maintain $\sim 900 \text{ mAh g}^{-1}$ after 1100 cycles. The downfall to this procedure is the high cost of production and materials used to make germanium nanowires [26].

Alloys of materials can have different theoretical capacities than their pure counterpart. While pure germanium has a theoretical capacity of 1384 mAh g^{-1} , GeO_x have a theoretical capacity of 1250 mAh g^{-1} [20, 26]. This is also true for Sn and SnO_2 . SnO_2 has a theoretical capacity of 781 mAh g^{-1} while pure Sn has a theoretical capacity of 991 mAh g^{-1} [28, 29].

TiO_2 , as an anode material for LIBs, is environmentally benign and structurally stable. Nano-structured TiO_2 can greatly facilitate a faster lithiation/de-lithiation process because of its large specific area and short diffusion length. It was reported that titanium dioxide nanofibers can provide a stable cycling performance of 168 mAh g^{-1} for 50 cycles [13]. This capacity is much lower than commercially available graphite-based lithium ion batteries. It can be paired with materials containing higher theoretical capacities to help form stable SEI layers. Jeong paired TiO_2 with mesoporous carbon and silicon nanoparticles (Si NP) [13]. He created a core-shell nanofiber using a mixture of mesoporous carbon and TiO_2 as the outer shell and Si NP as the inner shell. This composite allowed for a cycling performance of 939 mAh g^{-1} at a high current density of 12C [13]. Jeong has the same issue as Kennedy, i.e. the mesoporous carbon is very expensive, leading to an increase in fabrication cost for practical applications.

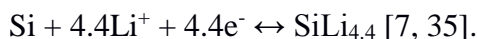
TiO_2 nanofibers have also been paired with SnO_2 . This pairing has a capacity of 781 mAh g^{-1} [29]. During the lithiation process, the volume of tin can expand by almost 200% compared to its original size, thus leading to pulverization and quick degradation of the high capacity [9, 29]. When SnO_2 is combined with structurally stable TiO_2 , the cycling performance is able to be

stabilized to a certain degree. Our group used a facile fabrication method to obtain SnO₂/TiO₂ composite nanofibers with a capacity of 610 mAh g⁻¹ [29]. Another group was able to get a capacity of 445 mAh g⁻¹ by encapsulating SnO₂ nanoparticles inside TiO₂ nanowires [9].

A novel idea was proposed by Chen from Shanghai University where microwave thermal synthesis and one step hydrogen gas reduction was used to create Sn/graphite nanocomposites [30]. These composite nanomaterials were able to hold a specific capacity of 946 mAh g⁻¹ after 30 cycles and this method is suitable for large scale fabrication and thus lowering the fabrication cost. This, however, was done at 0.1C which means that it took 10 hours to charge to its full capacity. When the C-rate was increased, the capacity dropped dramatically [30].

1.5 Advantages and disadvantages of silicon in Lithium Ion Batteries

When Si is used as an anode material in lithium ion batteries, it undergoes a 300% volume expansion like that of Sn [31, 32]. Silicon can fracture and thus cause the reformation of the solid electrolyte interface layers, leading to the rapid degradation of LIBs. Solid electrolyte interface (SEI) layers are formed during the first several cycles of lithiation [33]. SEI layers represent a major role in the outcome of the battery's performance which includes its cycle life, safety, coulombic efficiency and the irreversible capacity loss [33, 34]. Si can go through the following reaction during the lithiation process:



This results in an impressive capacity as high as 4200 mAh g⁻¹. In the case of silicon anode, SEI layers are mainly composed of SiO₂ and Li_xSiO_y using LiPF₆/EC-based electrolytes [14]. Silicon micron-powders are extremely challenging to work with. This is mainly due to its poor mechanical strength, which can cause pulverization and rapid capacity degradation during repeating lithiation/de-lithiation processes. One group at Stanford University, however, utilized a self-healing

polymer to patch the cracks formed during the lithiation/delithiation process of micron-size silicon [36]. The group got the idea for the self-healing polymer from the environment because it is an important survival tool for some living creatures. This group used a liquid self-healing polymer made up of branched hydrogen-bonding amorphous polymer with a low glass transition temperature to heal the cracks in the silicon material unrestrictedly and constantly at room temperature [36]. The self-healing property is due to hydrogen bonding occurring between individual polymer strands. This can be seen in the chemical structure of the compound (Figure 5). The specific capacity they obtained was 3,200 mAh g⁻¹ at 0.2C for 25 cycles [36]. Another research group used micron-sized Si particles to form Si nanoparticles after repeating lithiation/delithiation. They then used “conductive polymer binder PFM over the insulating PVDF to replace nonbonding acetylene black” [37]. They were able to obtain a high capacity of 2,500 mAh g⁻¹ after 30 cycles with a retention rate of 73% [37].

Another way to use micron-sized Si is by using a SiO material. Si et al. used ball-milled SiO and carbon nanofiber composite for LIBs. SiO was pulverized using high energy mechanical milling for 12 hours with carbon nanofibers producing a composite electrode material. This electrode produced an initial discharge capacity of 724 mAh g⁻¹. It only degraded to 675 mAh g⁻¹ after 200 cycles at 0.1C [38]. Using micron-sized silicon particles can significantly reduce the fabrication cost by at least one order of magnitude, but their cycling performance needs to be significantly improved for practical applications.

1.6 Nanoscale silicon for Lithium Ion Batteries

Nanotechnology can play a critically important role for silicon to be applied in high performance LIBs. Hitachi Maxell’s cell employs SiO material commercially as part of their anode composition [13]. One big advantage is nano-dimension decreases the time it takes to charge a

battery due to the decrease in the size dimensions. This can be explained using the diffusion equation:

$$l = \sqrt{Dt}.$$

The D is the diffusion coefficient which is a constant for a specific material at constant temperature. l is the radius of the silicon powders and t is the diffusion time. By decreasing the size, one can decrease the time it takes to charge silicon powders. This property is extremely important in terms of enhancing the C-rate performance, especially when the material does not have a high electrical conductivity. Nanoscale Si particles still have the 300% volume expansion. However, the mechanical strength of nanoscale Si is much higher than its micro-sized counterpart. This allows for such a high volume expansion. Si can be fabricated into multiple types of nanomaterials: nanowires, nanocrystals, nanotubes, nanospheres, nanofibers, and nanoporous materials [37]. Our group started with Si micron-sized particles and made a Si/C/TiO₂ composite nanofibers [32]. These nanofibers allowed for a specific capacity of 720 mAh g⁻¹ after 55 cycles with a retention rate of 94% [32]. Jeong used a core-shell method to encapsulate silicon nanoparticles within TiO_{2-x}/mesoporous carbon composite microfibers [13]. These composite microfibers had an initially high capacity of 939 mAh g⁻¹ at 0.2C. Another group started with a Si nanoscale building blocks then coated them with carbon to create micron-sized Si-C networking composites [34]. The carbon coating reduces the formation of HF which reacts with current collectors, leading to a fast degradation of LIBs. This combination allowed for a specific capacity of 1200 mAh g⁻¹ for 600 cycles, but the fabrication cost is extremely high [34].

Luais et al. used a 5 μm thin silicon mesoporous film for LIBs, which was obtained by etching a silicon wafer. These pores range in diameters from 60 to 70 nm. This method allowed

for an initial capacity of 1910 mAh g⁻¹ (C/9) which degraded to 1860 mAh g⁻¹ on the 70th cycle then to 1485 mAh g⁻¹ at the 150th cycle [39]. Although the gravimetric capacity is very high, this method can hardly be scaled up easily due to the use of expensive silicon wafer and complicated fabrication method.

Jing et al. formed a novel coral-like surface Si nanowire array (SNWA) on copper foam for use in LIBs [40]!. Conventional SNWA (c-SNWA) anodes have a structural instability during lithium insertion. The novel approach they have come up with shows a higher structural stability during lithation. C-SNWA have a reversible capacity of 127 mAh g⁻¹ at 3200 mA g⁻¹ while novel SNWA (n-SNWA) have a reversible capacity of 2178 mAh g⁻¹ at 400 mA g⁻¹ for 50 cycles [40].

Simon et al. used silicon coated carbon nanofiber to improve lithium ion batteries performance. A chemical vapor deposition method was used to coat carbon fiber mesh with silicon. This type of electrode demonstrated an initial capacity of 954 mAh g⁻¹, but faded to 766 mAh g⁻¹ after 20 cycles at a fixed current density of 50mA g⁻¹ [7]. Si et al. out of Mie University also used a coating method to increase the cycling performance of silicon-based lithium ion batteries. This group used a composite of nano-Si powder and pyrolytic carbon of polyvinyl chloride (PVC) with carbon nanofibers. They began by coating nano-Si powder with carbon by pyrolyzing PVC and then mixed it with CNF using a rotational mixer. The initial charging capacity was 2186 mAh g⁻¹ decreasing to 2128 mAh g⁻¹ at the 3rd cycle after the SEI layer formation. On the 40th cycle, the specific capacity decreased to 1073 mAh g⁻¹ [41]. Starting with nanosized materials allows for less possibility of cracking and leaching into the electrolyte and reformation of the SEI layers.

Chapter 2: Silicon Encapsulated in TiO₂ Nanofibers

2.1 Introduction

Titanium dioxide nanomaterials possess the advantages of low-cost, structural stability, environmentally benign, large surface area and ease of processing via sol-gel method [35, 42, 43]. But TiO₂ has a very low theoretical specific capacity for all of its three phases: anatase, rutile, and brookite. The rutile phase provides the highest capacity of 335 mAh g⁻¹ (Li_{0.85}TiO₂) followed by anatase at 310 mAh g⁻¹, and finally, brookite has the lowest with 282 mAh g⁻¹ [32, 44]. Noteworthy, lithium ions can only be inserted into anatase lattice via a special direction due to its unique crystal structure, thus leading to a highly poor rate performance. In contrast, silicon has an impressive capacity of 4,200 mAh g⁻¹ (Li_{4.4}Si), yet its operational voltage is quite low, thus benefiting a higher power density [7]. However, the structure of silicon is quite unstable mainly due to the nearly 300% volume change during the lithiation/de-lithiation process [8, 29]. Here, silicon nanoparticles of a high specific capacity are confined in the structurally stable titanium dioxide (TiO₂) nanofiber matrix, which is employed as an anode material in lithium ion batteries. These nanomaterials possess the advantages of high capacity, high structural stability, low-cost and excellent rate and cycling performance. The sulfur is added to the matrix as a template to aid in the creation of void structures within the TiO₂ fibers to accommodate the nearly 300% volume variation during the Si lithiation and de-lithiation processes (Figure 6). Carbonization was performed on the nanofibers to increase the amount of amorphous carbon within the sample. Amorphous carbon does not aid in the capacity of the battery, but better improves the conductivity of these samples. [45]

Five types of nanofibers (NFs) were fabricated: pure titanium dioxide (TiO₂) and 4 composite nanofibers. Composite nanofibers were labeled as SiNP/TiO₂, SiNP/TiO₂ with S as a template, SiNP/C/TiO₂ NF, and SiNP/C/TiO₂ with S as a template. Labeling of these samples such

as SiNP/C/TiO₂ NF with S as a template means that Si nanoparticles were encased in a titanium dioxide matrix and sulfur was added as a template. This sample was carbonized which is indicated by the “/C/” within the label. If the “/C/” is not present within the label, the sample was not carbonized. This is the same as if the “with S template” is absent that means that the sample did not have sulfur in the nanofiber. These NFs were then fabricated into LIB anodes for electrochemical performance tests. A diagram of this procedure is shown in Figure 7. It should be pointed out specifically that the electrochemical performance of NFs is very poor if they are annealed in air instead of being carbonized in helium, mainly due to the oxidation of silicon NPs. The procedures for making these nanofibers were described as followed

2.2. Experimental

The whole experimental design consists of nanofiber fabrication, nanofiber characterization, battery assembly, and battery tests.

2.2.1 Chemicals

Polyvinylpyrrolidone (PVP) was purchased from Sigma Aldrich at a molecular weight of 1.3M. Ethanol (EtOH) was acquired from Pharmco. Inc. at a purity level of 99.9%. 98% titanium isopropoxide (TiIP), 99.8% sublimed sulfur, and 99% acetic acid (HOAc) was procured from Acros Organics. The N-methyl-2-pyrrolidone (NMP) that was used as a solvent in the slurry preparation was purchased from Sigma Aldrich at >99.5% solution. Crystalline silicon nanoparticles (SiNP), of less than or equal to 50nm in diameter and a purity of 98%, were purchased from Alfa Aesar where they were laser synthesized from vapor deposition. The MTI Cooperation provided materials for electrode preparation and battery assembly. This included the polyvinylidene fluoride (PVDF) binder, carbon black, copper foil roll for the electrode, negative

cases, positive cases, springs, steel spacers, lithium metal, polyethylene/polypropylene membrane roll with pore size 20-30 nm, and LiPF₆ electrolyte in EC/DMC/DEC 1:1:1 in volume.

2.2.2 Instrumentation

Characterization and the overall experimental design could not have been carried out without the aid of many instruments and resources. In order to electrospin the nanofiber, a NE300 syringe pump with 12V DC at 0.75A and a Series 230 Bertan High Voltage Power Supply were utilized. For annealing and carbonization, a tube furnace by Lindberg/Blue M was used. Nanofibers were characterized using Brunauer-Emmett-Teller Surface Area Analysis (BET), Barrett-Joyner-Halenda (BJH) pore size distribution analysis, Scanning Electron Microscope-Energy Dispersive Spectroscopy (SEM-EDS), Transmission Electron Microscopy (TEM), powdered X-Ray Diffraction (XRD), Raman Spectroscopy, and Thermogravimetric Analyzer (TGA). BET and BJH measurements were performed on a Micromeritics ASAP 2020 Surface Area and Porosity Analyzer using N₂ as an adsorption gas and ASAP2020 V4.02 software. SEM-EDS and TEM was completed using the JSM7600F model of the SEM-JEOL SEM with a transmission electron detector (TED). Powdered XRD was performed on the MiniFlex 600 model manufactured by Rigaku with a Cu k_α of 1.54Å at Armstrong State University. The Raman spectra were obtained using the DXR Raman Microscope model manufactured by Thermo Scientific. The laser power was 3.0 mW of 532 nm. The exposure time was 50 seconds using an object lens of 10X magnification and a pinhole aperture of 50 μm. While using TA Instruments TGAQ50 model, TGA data was able to be acquired. Resistance was measured using a DM110 Pocket Multimeter by EXTECH instruments. Testing on the fabricated batteries was done using the VMP3 model from BioLogic potentiostat with 110-240Vac power at 50/60Hz and EC Lab V10.32 software with an operation window of 0.01-1.5V vs. Li/Li⁺.

2.2.3 Fabrication of Titanium Dioxide Nanofibers (TiO₂ NF)

The fabrication of titanium dioxide nanofibers (TiO₂ NF) began with mixing ~1 gram of PVP with 10 mL of ethanol. In a separate container ~3 grams of TiIP was mixed with 5 mL of ethanol and 3 mL of Acetic Acid. These solutions were vortexed separately for ~ 30 minutes to ensure thorough mixing. The solutions were then added together and vortexed again for another 5 minutes. This mixture was then sonicated for 20 minutes before electrospinning [35].

2.2.4 Fabrication of Silicon Nanoparticle (NP)/ Titanium Dioxide Nanofibers (SiNP/TiO₂ NF and SiNP/C/TiO₂ NF)

The fabrication of silicon nanoparticle/ titanium dioxide (SiNP/TiO₂ NF and SiNP/C/TiO₂ NF) nanofibers began with the mixing of ~3 grams TiIP, 1 gram of silicon nanoparticles, 3 mL Acetic Acid and 5 mL of ethanol. In another separate container, 1 gram of PVP and 10 mL of ethanol was mixed. Both mixtures are vortexed for ~30 minutes. The solutions were then combined and vortexed again for another 5 minutes. The sol-gel was then sonicated for 20 minutes before electrospinning [35].

2.2.5 Fabrication of Silicon Nanoparticle/ Titanium Dioxide Nanofibers with Sulfur as a template (SiNP/TiO₂ with S as a template and SiNP/C/TiO₂ with S as a template)

2.5 grams of sulfur and 1 gram of silicon nanoparticles were mixed and ground using a mortar and pestle. This combination was then mixed with 3 g TiIP, 5 mL of Ethanol, and 3 mL of Acetic Acid. In another vial, 10 mL ethanol and 1 gram of PVP were mixed. Both vials were then separately vortexed for 30 minutes. These two vials were combined and vortexed for another 5 minutes, and then the sol-gel was sonicated for 20 minutes before electrospinning [35].

2.2.6 Electrospinning and Post-treatment

Once the gelation of the intended nanofiber was completed, it was ready for electrospinning. The parameters of electrospinning were as follows: the distance from the end of the syringe to the grounding aluminum collector was 12-15 cm. The pumping rate of sol-gel solution was 5 mL/hr. The applied DC voltage was 25 kV. A schematic of this process is shown in Figure 8. Once all the sol-gel solution had been electrospun, fabricated fibers were left overnight for complete gelation. These nanofibers were either annealed at $\sim 565^{\circ}\text{C}$ in air for roughly 12 hours or were carbonized with a helium gas protection at 800°C for four hours [35].

2.2.7. Battery Fabrication and Battery Test Conditions

The first step of battery fabrication was to make slurry using nanofibers or Si NPs. The slurry contains 80% w/w of nanofibers, 10% carbon black, and 10% PVDF binder in NMP. The second step was to sonicate for 2 hours to make sure the materials were well dispersed. The slurry was then coated on 15 mm diameter Cu disks to make the desired electrode. Copper disks were used as a current collector for anode in LIB. It is important to make sure the entire Cu foil was coated as evenly as possible. The disks were then placed in a vacuum oven and heated at 100°C overnight to remove solvent and any residual moisture.

In the next step, the electrode was assembled into half-cells using lithium metal [MTI Cooperation] as the counter electrode in a glove box with a well-controlled concentration of O_2 and H_2O ($< 1\text{ppm}$). $60\ \mu\text{L}$ of LiPF_6 electrolyte in EC/DMC/DEC 1:1:1 in volume was added atop the active material electrode. The membrane separator that was placed between the active material electrode and counter electrode of lithium metal. A steel spacer and spring was placed on top of the counter electrode to increase contact due to the softness of Li metal. This fabrication process is portrayed in Figure 3. The coin cell battery was crimped together under 100lbs of force and wiped clean of any excess electrolyte that leached out during the compression [35].

TiO₂ NFs, SiNP, SiNP/TiO₂ NFs, SiNP/C/TiO₂ NFs, SiNP/TiO₂ NFs with S as a template, and SiNP/C/TiO₂ NFs with S as a template were assembled into 2032 type coin cells. Their electrochemical properties, including cycling performance and voltage profile, were measured (Figure 15, 16, and 17) using a potentiostat. The batteries were charged and discharged between 0.01-2.0 V applying a constant current. The specific capacity versus the cycle number is plotted for these batteries in Figures 15 and 16 [35].

2.3 Results and Discussion

2.3.1. Characterization

BET was used to determine the specific surface area of nanofibers. The purpose of using the SEM-EDS is to obtain surface morphology and percent composition of the nanofibers. Obtaining the percent composition is important in determining the theoretical capacity of each battery fabricated. The TGA assists in determining the concentration of carbon in each nanofiber, and EDS can be utilized to determine the mass ratio of silicon to TiO₂. The XRD and Raman can provide phase information of these nanomaterials. BET data in Table 1 shows that the specific area of noncarbonized pure TiO₂, SiNPs/TiO₂, and SiNP/TiO₂ with S template using nitrogen as adsorption gas. In contrast, the surface areas of carbonized samples are significantly higher as shown in Table 2. The carbonized SiNP/C/TiO₂ NF with S as a template has the highest surface area. It is almost 5 times higher than the surface area of carbonized SiNP/C/ TiO₂ NF. This is due to the porous nature of the nanofibers, as further confirmed by SEM and TEM data [35]. The pore size distribution of carbonized SiNP/C/TiO₂ NF with S as a template was analyzed using a well-known BJH model installed in the software. This model is suitable for pore sizes 2-50 nm with a cylindrical geometry.[46] The pores in carbonized SiNP/C/TiO₂ NF with S as a template have a broad distribution ranging from 0.9 to 150 nm, 63% whose total pore volume was contributed from

pores with sizes 1-6 nm. It is not surprising to have such a broad size distribution, considering the composite NFs have a very complex structure consisting of nanoparticles, nanofibers and nanopores. Thus, the pore size distribution derived from BJH model may be different from the real scenario.

SEM imaging was performed on carbonized SiNPs, TiO₂, and SiNPs/C/TiO₂ nanofibers, as well as carbonized SiNPs/C/TiO₂ NF with sulfur as the template and noncarbonized SiNP/TiO₂ with S as a template (Figure 9). The SiNPs/C/TiO₂ NFs prepared using S as the template have an average diameter of 482 ± 143 nm, as shown from the histogram data in Figure 10. The diameters of carbonized TiO₂ NFs are quite uniform (237 ± 85 nm) and so are the carbonized SiNPs/C/TiO₂ nanofibers (225 ± 65 nm) (Figure 10). It is interesting that there were apparently no fibers in the SiNPs after carbonization (Figure 9b). This is due to the lack of cross-linking sol-gel chemistry. There are many nanoparticles aggregated on the surface of SiNP/C/TiO₂ NFs (Figure 9c). For the carbonized SiNP/C/TiO₂ NFs with sulfur as the template, there are much fewer aggregations of SiNPs on the surface. A noteworthy observation is that these fibers are much shorter than those of carbonized TiO₂ NFs (Figure 9a and 9e). This can be explained by the hindrance of SiNP on the crosslinking sol-gel chemistry, resulting in shorter fibers. Also to note, are the differences between the noncarbonized and carbonized sulfur templated samples (Figures 9d and 9e). The carbonized samples are much shorter and thicker than the noncarbonized samples with smaller conglomerations of NPs [35].

To further determine if the carbonized SiNP/C/TiO₂ NFs with S template truly was as porous as indicated by the BET data, a magnified SEM image was taken as shown in Figure 11a. TEM was also utilized to confirm the porous structure of these NFs (Figure 11b). The zoomed-in SEM image shows cracking along the nanofiber surface. This void structure can efficiently

accommodate the fractured silicon NPs formed during the lithiation of the SiNPs trapped within the TiO₂ NFs, thus significantly improving its cyclability. The TEM image shows the trapped silicon particles (dark spots within the fiber circled in red) and the cracks/void space (circled in light blue) that were observed in the up-close SEM image [35].

Powder XRD patterns were measured at Armstrong State University with the help of Dr. Clifford Padgett (Figure 12). Powder XRD patterns at 28°, 36° and 54° are from the (110), (101), and (211) crystal planes of rutile TiO₂ (JCPDS No.:41-1487), respectively (Figure 12a and 12b). The broad pattern at 63° is from the (002) and (310) crystal planes of rutile TiO₂ [32, 35, 47, 48]. There are also patterns from anatase TiO₂ at 25° from the (101) crystal plane and 41° from the (112) crystal plan in the carbonized SiNP/C/TiO₂ NF with S template sample [32, 35, 47, 48]. The carbon in the carbonized sample is amorphous because no sharp diffraction peak was observed at 26°. Graphite has a distinct peak at 26° from the (002) crystal plane (JCPDS No.: 41-1487) [32, 35, 49]. The (111) cubic phase silicon diffraction pattern is evident by the peak at 27° along with the (220) pattern at 47°, the (311) at 56°, and the (400) at 69°. (JCPDS No.: 27-1402) [32, 35, 49, 50].

Raman data further confirmed the existence of cubic silicon and rutile TiO₂ in these samples (Figure 13). Three distinct peaks can be seen for the rutile TiO₂: 141, 442, and 607 cm⁻¹. The B_{1g} peak of rutile TiO₂ can be observed around 141 cm⁻¹ which is consistent with the literature reported value. The A_{1g} peak of rutile TiO₂ can be found around 607 cm⁻¹ and is also consistent with literature values, and the peak around 442 cm⁻¹ is credited to the E_g peak of rutile TiO₂ [29, 35, 51, 52]. Si transverse photon scattering is the culprit of the Raman shift at 516 cm⁻¹ [35, 53]. The carbon in the carbonized samples was in the amorphous form because there was no presence of D-band at 1370 cm⁻¹ or G-band of graphite at 1580 cm⁻¹ in their Raman spectra [35, 54, 55].

Determining this is important because amorphous carbon does not provide additionally capacity to the battery while graphite would. The Raman data are consistent with powder XRD data as described above. To summarize all the characteristic data findings, carbonized SiNP/C/TiO₂ NF with S template has porous structure with a large surface area. These NFs consist of cubic Si, rutile TiO₂ phases and amorphous carbon.

Finally, TGA was used to determine the percent composition of carbon within the carbonized samples (Figure 14). TGA data of carbonized SiNP (Figure 14b) indicate that there is 8% carbon in the sample. Carbonized TiO₂ and SiNP/C/TiO₂ NFs experienced 14% and 17% weight loss respectively, due to the oxidation of carbon materials (Figure 14 a and c). The increase in percent weight in figures 14b and 14c, can be attributed to oxidation of Si within the carbonized SiNP and SiNP/C/TiO₂ NF samples. 34.2% of the carbonized SiNP/C/TiO₂ NFs with sulfur as the template was carbon (Figure 14 d). The mass percentage ratio of TiO₂ to Si to C was then determined to be 55.6%: 10.2%: 34.2% after further energy dispersive spectra (EDS) elemental analysis. For example, in order for get the mass percent of silicon the equation:

$$\%Si = (100 - \%C_{TGA}) * (\%Si_{EDS}) / (\%Si_{EDS} + \%Ti_{EDS} * FW \text{ of } TiO_2 / AW \text{ of } Ti)$$

$$\%TiO_2 = (100 - \%C_{TGA}) * (\%Ti_{EDS} * FW \text{ of } TiO_2 / AW \text{ of } Ti) / (\%Si_{EDS} + \%Ti_{EDS} * FW \text{ of } TiO_2 / AW \text{ of } Ti)$$

The theoretical capacity contributed from active material silicon and TiO₂ can be calculated using the following equation:

$$(Theoretical \ Capacity = (0.102 / (0.556 + 0.102)) \left(4200 \frac{mAh}{g} \right) + (0.556 / (0.556 + 0.102)) \left(335 \frac{mAh}{g} \right)) \text{ [52].}$$

This is the addition of the percent composition of TiO₂ and Si determined using EDS and TGA data multiplied by their respective theoretical capacities [35]. It should be pointed out specifically

that amorphous carbon can be completely oxidized below 600°C in air and only negligible amount of Si NPs can be oxidized at 600°C as shown in Figure 14e. Significant oxidation of Si NPs doesn't occur until 800 °C. Given there is only ~10% wt Si in our composite NFs, the mass increase below 600 °C due to Si oxidation is highly trivial. However, this insignificant oxidation can increase the thickness of insulating silica layer on Si NPs, resulting in a poor electrochemical performance of LIBs made from NF samples annealed in air (Figure 15a), which will be discussed later in this chapter.

2.3.2. Electrochemical Performance

Cycling performance and voltage profiles are two important electrochemical characteristics of LIBs. Cycling performance is important because it shows stability and capacity of LIBs. Voltage profiles contain information related to what materials within each of the sample contribute to overall battery capacity.

Cycling performance and coulombic efficiency analyses were carried out on non-carbonized samples of SiNP, SiNP/TiO₂, and SiNP/TiO₂ with S as a template (Figure 15 a and b). Coulombic efficiency is the ratio of the charge released to the charge input during each cycle. It is a parameter describing the reversibility of electrochemical reaction. The overall specific capacity of non-carbonized SiNPs was initially high, 2370 mAh g⁻¹ after three formation cycles at 0.122 A g⁻¹, but rapidly degraded to 36 mAh g⁻¹ after 100 cycles (Figure 15a). Notably, the initial capacity is lower than the theoretical value of silicon, 4200 mAh g⁻¹, due to the agglomeration of silicon NPs [56]. The poor cycling performance is due to the structural instability of this material. Recall that there is nearly 300% volume expansion during the silicon lithiation process [8, 29]. The volume expansion can pulverize SiNPs and result in unstable SEI layers, thus limiting the stability of the battery. Non-carbonized TiO₂ has a specific capacity of 69 mAh g⁻¹ and remains stable for

100 cycles at 0.117 A g^{-1} . Outstandingly, the capacity of TiO_2 NFs has been increased slightly up to 83 mAh g^{-1} after 100 cycles. Non-carbonized SiNP/ TiO_2 NF had a low capacity of 140 mAh g^{-1} and remained stable throughout the 100 cycles at 0.083 A g^{-1} (Figure 15a). It is believed that the majority of this capacity is contributed from TiO_2 and Si NPs have been significantly oxidized. This was partially proven by comparing the resistance of the annealed SiNP to original SiNP. Using a multimeter, original SiNP thin film, sandwiched between two gold thin film electrodes, provided a resistance of 13-20 $\text{M}\Omega$. While annealed SiNP's resistance was above 100 $\text{M}\Omega$. This proves that the annealed SiNPs were significantly oxidized at elevated temperature in air, resulting in the formation of thick insulating silica layer on Si NP and thus low capacity. Non-carbonized SiNP/ TiO_2 with S template had a starting capacity of 339 mAh g^{-1} at 0.508 A g^{-1} . This capacity degraded by only 28% to 177 mAh g^{-1} after 100 cycles (Figure 15a). The capacities of these batteries were lower than commercially available graphite-based batteries. We believe that such a poor capacity is mainly caused by the rapid oxidation of silicon at nanoscale. So our group progressed to carbonization, purposing to preventing the oxidation of SiNPs and thus increasing the electrical conductivity of these NFs [56].

When cycled at a constant current density of 0.09 A g^{-1} , carbonized TiO_2 NFs exhibited a capacity of 162 mAh g^{-1} after the first three cycles. This capacity only dropped by 12% compared to the initial starting capacity after 100 cycles, indicating stable SEI layer formation on the surface of TiO_2 . Compared to non-carbonized TiO_2 NFs, carbonized TiO_2 NFs have a higher electrical conductivity due to the presence of electrically conductive carbon (TiO_2 is a wide bandgap semiconductor), thus leading to an enhanced specific capacity. At 0.135 A g^{-1} , the specific capacity of carbonized SiNP/C/ TiO_2 NFs had a capacity of 625 mAh g^{-1} with only 21% capacity retention after 100 cycles. After the formation of the SEI layers, a 0.018 A g^{-1} constant current density was

added to the carbonized SiNPs, which showed a very high initial capacity of 1338 mAh g⁻¹. This rapidly degraded to 17 mAh g⁻¹ after 100 cycles (Figure 16). SiNPs do not reach their theoretical capacity (4200 mAh g⁻¹) due to the agglomeration of these nanoparticles after the annealing process at high temperatures (Figure 9a) [35].

In contrast, SiNP/C/TiO₂ NFs with sulfur as the template initially demonstrated a much higher overall capacity of 839 mAh g⁻¹ with a current density of 0.135 A g⁻¹. 50% of the initial capacity was retained after 180 cycles. The higher capacity compared to the TiO₂ NFs was credited to the capacity contribution from SiNPs. The presence of sulfur in the carbonized SiNP/C/TiO₂ NFs with S as a template before it was removed also protected the Si from being oxidized. The contribution of Si in the carbonized SiNP/C/TiO₂ NF with sulfur as the template was established by the voltage profile with the presence of a plateau at 50 mV observed in both samples (Figure 17) [32]. In addition, a small plateau can be found around 1.25 V in TiO₂ and SiNP/C/TiO₂ with S as the template arose from the irreversible phase transformation from TiO₂ to LiTiO₂ [32, 35, 57, 58].

The carbonized SiNP/C/TiO₂ NFs with S as a template at 0.135 A g⁻¹ showed excellent cyclability of a 54% overall capacity retention after 180 cycles. If the TiO₂ capacity contribution was subtracted and the remaining capacity was assumed to be completely from SiNPs which was normalized to the mass of Si NPs, it results in Si NPs demonstrated an exceptional capacity of 3459 mAh g⁻¹ after the SEI layer formation (Figure 18). This is terribly close to the theoretical capacity of silicon reported in literature [32]. This capacity gradually decreased to 1800 mAh g⁻¹ after 80 cycles and stabilized after that to 180th cycle (1586 mAh g⁻¹). The coulombic efficiency of the sample stays ~100% through all the cycles thus further proving the stability of the battery (Figure 18) [35].

Outstanding rate performance was demonstrated by the carbonized SiNP/C/TiO₂ NFs with S as a template as shown in Figure 19. More than 55% capacity was obtained when increasing the C-rate from 0.1 C to 0.8 C [35]. It is shown that the electrode performance is comparable to that reported in literature even for some samples manufactured from refined methods. These refined literature methods can result in higher material fabrication costs. The electrospinning method, exploited in this work, is much more simplistic and can be scaled up with ease using multiple spinner techniques [35].

2.4. Summary

An original method to envelope SiNPs within the highly porous TiO₂ nanofiber matrix using sulfur as the template was developed to be able to accommodate the ~300% volume expansion during Si lithiation/delithiation process [35]. The electrospinning method utilized has a relatively low material cost and is simplistic enough that it can be easily scaled up. Carbonizing the samples provided better cycling performance and specific capacities than samples annealed in air. Carbonized SiNPs demonstrated a high initial specific capacity, however, it rapidly degraded, to 17 mAh g⁻¹ in 100 cycles [35]. TiO₂/C/SiNP using S as a template had an initial capacity of 839 mAh g⁻¹ at 0.135 A g⁻¹; 50% of this capacity was retained after 180 cycles. The specific capacity of silicon in these composite NFs can be maintained above 1586 mAh g⁻¹ even after 180 cycles at 0.135 A g⁻¹. In comparison, carbonized TiO₂ NFs can only provide a specific capacity of 143 mAh g⁻¹ after 100 cycles, its cycling performance was excellent though [35]. Another noteworthy observation was the ability to create porous nanofibers by using a more simplistic technique. Porous structures are a highly important research topic due to their broad applications in material science and engineering. It can be noted that the electrode performance of all our carbonized

materials is comparable to that reported in literature even for some samples synthesized from more sophisticated methods. The more sophisticated methods lead to an increase in fabrication cost.

Chapter 3: Concluding Remarks

The overall specific capacity of carbonized SiNP/C/TiO₂ using S as a template was relatively low due to the high content of TiO₂. Lowering the TiO₂ content by optimizing the precursor ratios resulting in a raise of the Si content will be attempted to further increase the capacity. Significant improvement in electrode performance is expected with optimization in electrode formula and fabrication, and electrolyte compositions [27]. Changing the carbonization temperature can also change the morphology of the nanofibers. This can aid in making the nanofibers more porous allowing for Si lithiation/delithiation. The ratios of PVDF, carbon black, and active composite nanofiber materials in the slurry are optimized for the electrode preparation for the enhancement of the battery capacity. Electrolytes can also play an important role in enhancing Si-based LIB performance. If the electrolyte has a higher ionic conductivity and does not react with the OH functional groups on Si NPs to release HF, the SEI layers will be more stable and have a more stable cycling performance.

This same research strategy can be applied to other high capacity anode materials like tin and germanium, which have a similar volume expansion problem during the lithiation process. . Creating porous nanofibers to encapsulate tin and germanium will prevent them from leaching out into the electrolyte, which can cause permanent and rapid capacity degradation. Many research projects are being conducted for the progress of lithium ion batteries, but more still needs to be done to make them commercially viable. In order to replace commercially available LIBs, new LIBs must be low in manufacture cost, have a high capacity, be light weight, and have a long cycle life. It is our dream that one day we will not need to charge our cell phones and laptops in two weeks, which theoretically is possible but has not been experimentally realized.

Figures

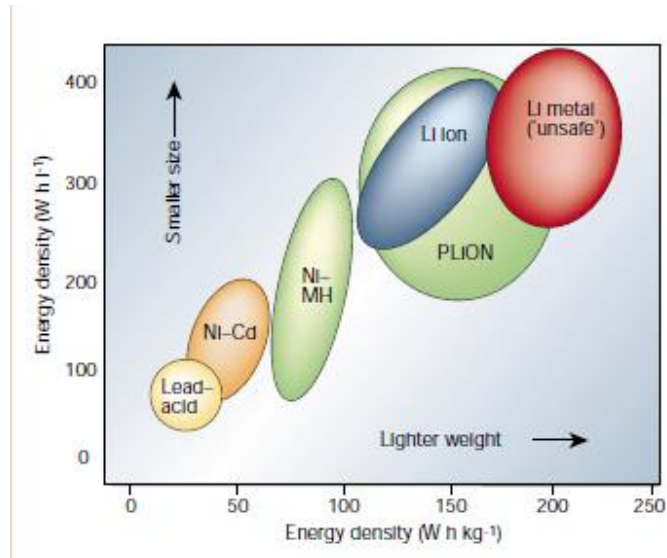


Figure 1: Comparison of lead-acid, alkaline and lithium ion batteries energy density of size versus weight.[5, 12]

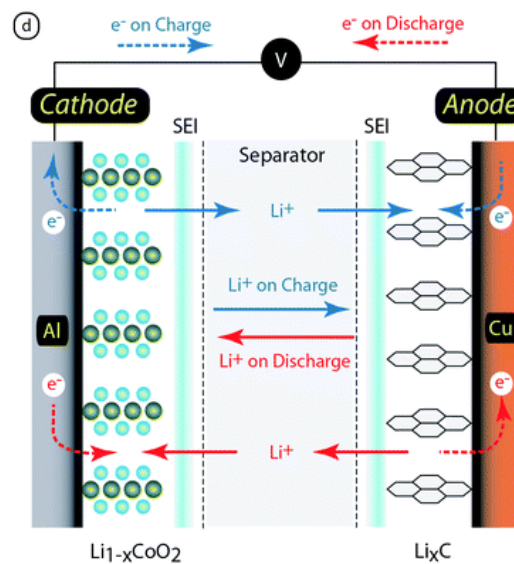


Figure 2: Lithiation and delithiation process of lithium ion batteries[12]

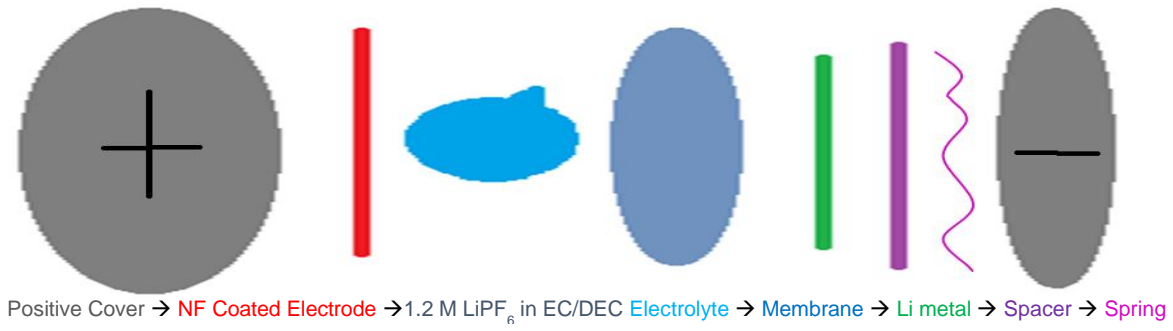


Figure 3: Internal schematic for lithium ion batteries

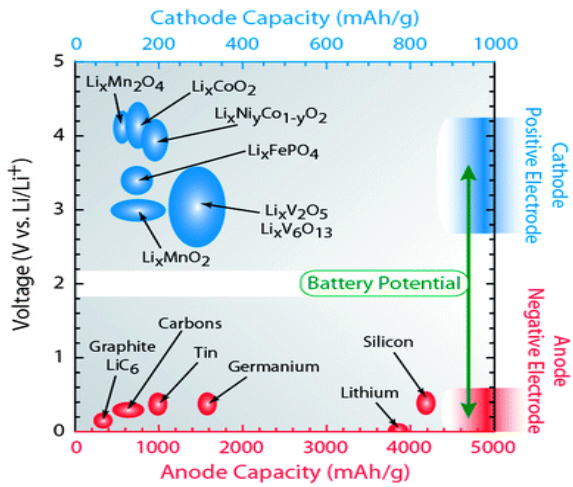


Figure 4: Anode and cathode materials for advanced lithium ion battery[12]

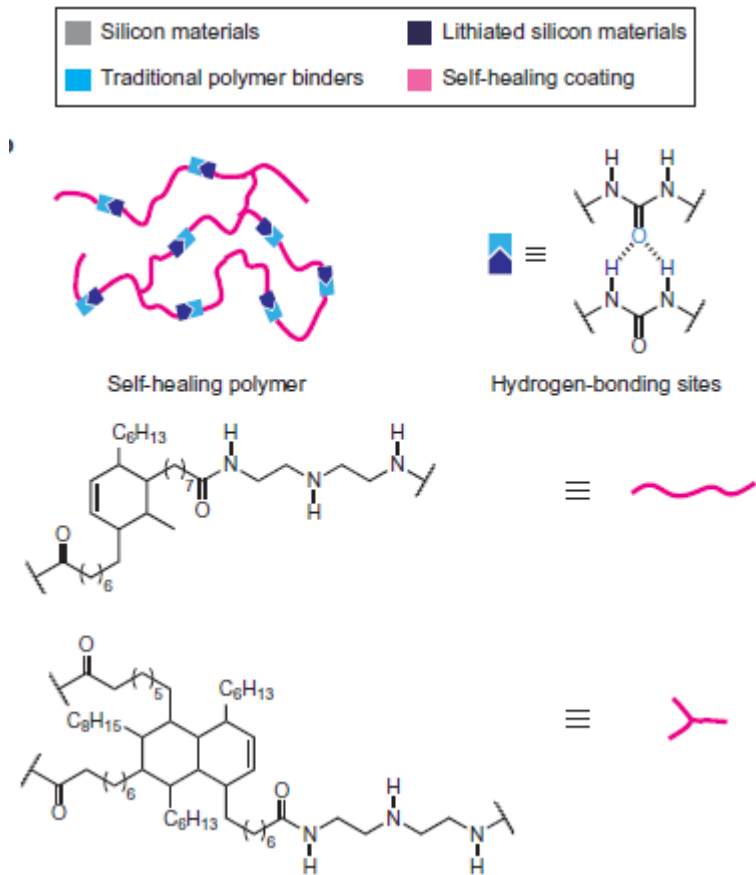


Figure 5: Molecular structure of the self-healing polymer.[36]

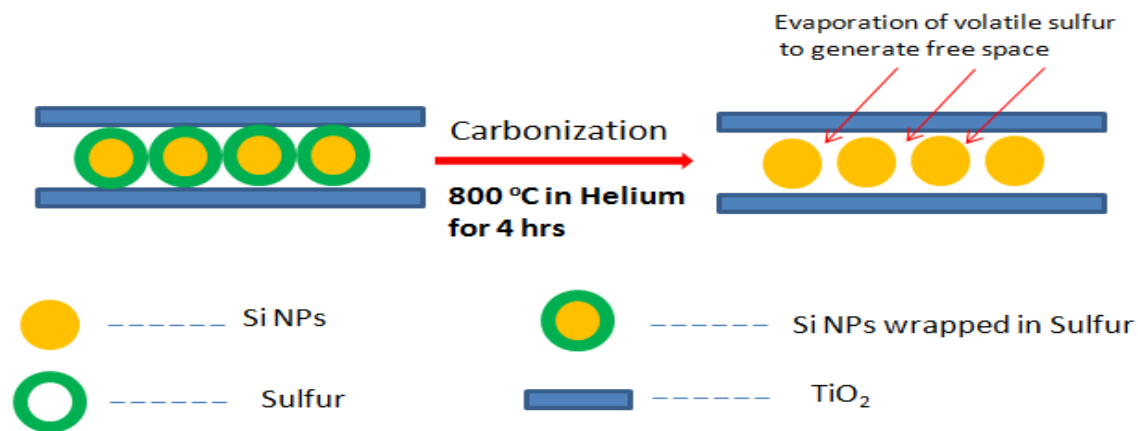
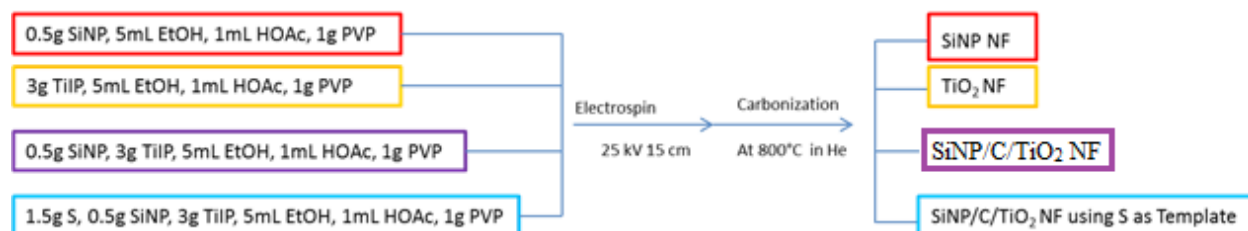


Figure 6: General schematic for the formation of void structure in SiNP/C/TiO₂ NF with S as a template.

General Procedure for Nanofiber Fabrication



HOAc: Acetic Acid; EtOH: Ethanol; PVP: Polyvinylpyrrolidone (1.3 M MW); SiNP: Silicon Nanoparticles; NF: Nanofibers; TiIP: Titanium Isopropoxide

Figure 7: General procedure for carbonized nanofibers.[35]

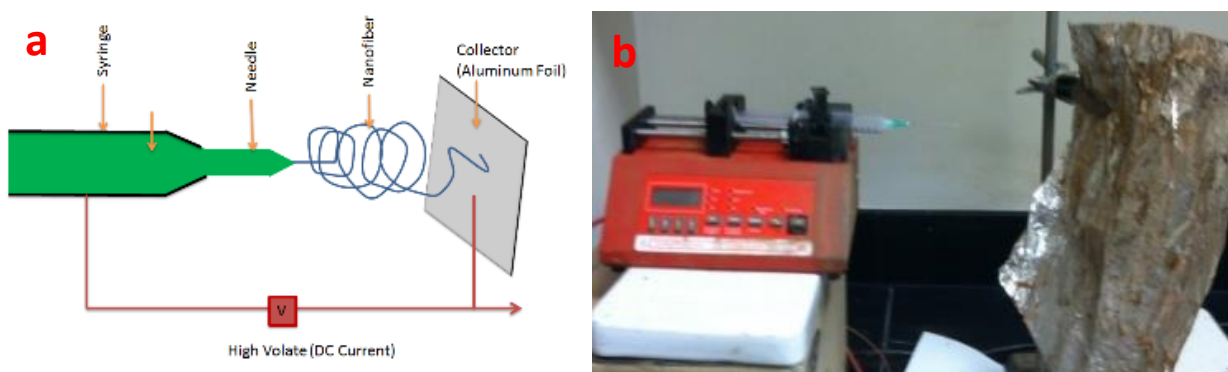


Figure 8: Fabrication method for processing nanofibers through sol-gel electrospinning: a) cartoon explanation and b) experimental set up.[29]

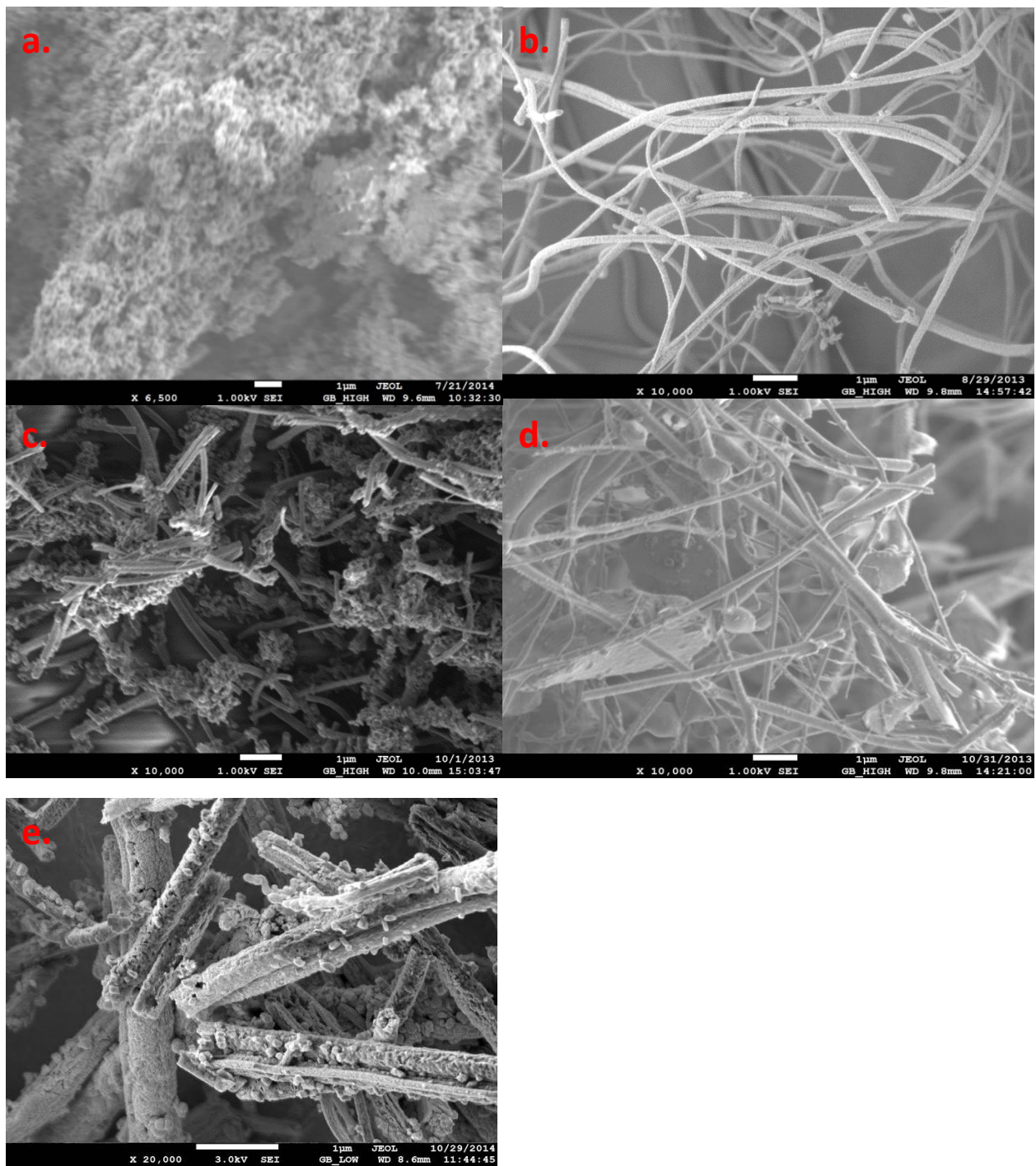


Figure 9: Scanning electron microscope images of a) carbonized SiNP, b) carbonized TiO₂ NFs, c) carbonized SiNP/C/TiO₂ NFs, d) noncarbonized SiNP/TiO₂ NFs with sulfur as a template, and e) carbonized SiNP/C/TiO₂ NFs with sulfur as the template.[35]

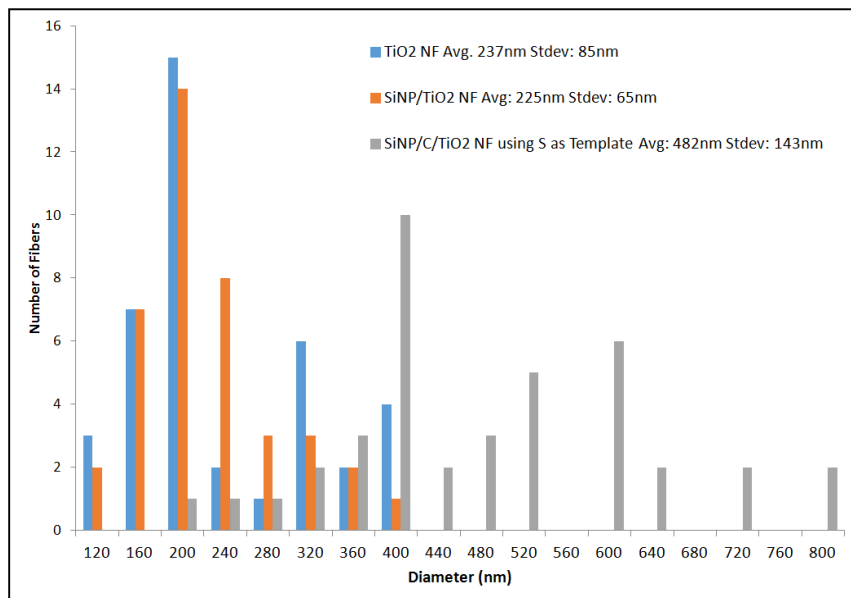


Figure 10: Histogram representation of the diameters of the carbonized TiO₂, SiNP/C/TiO₂, and SiNP/C/TiO₂ with S Template.

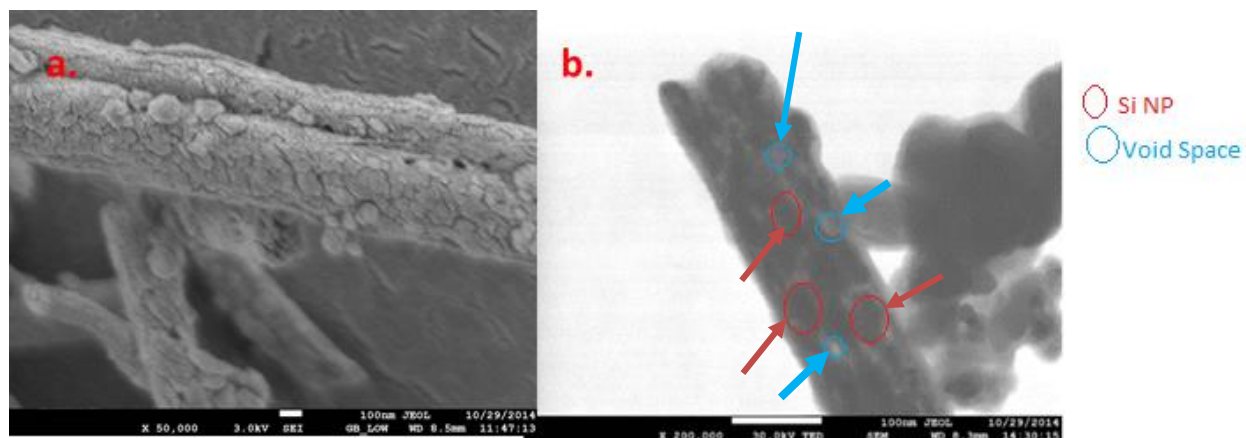


Figure 11: a) Magnified SEM image and b) TEM image of carbonized SiNP/C/TiO₂ NF with S as template[35]

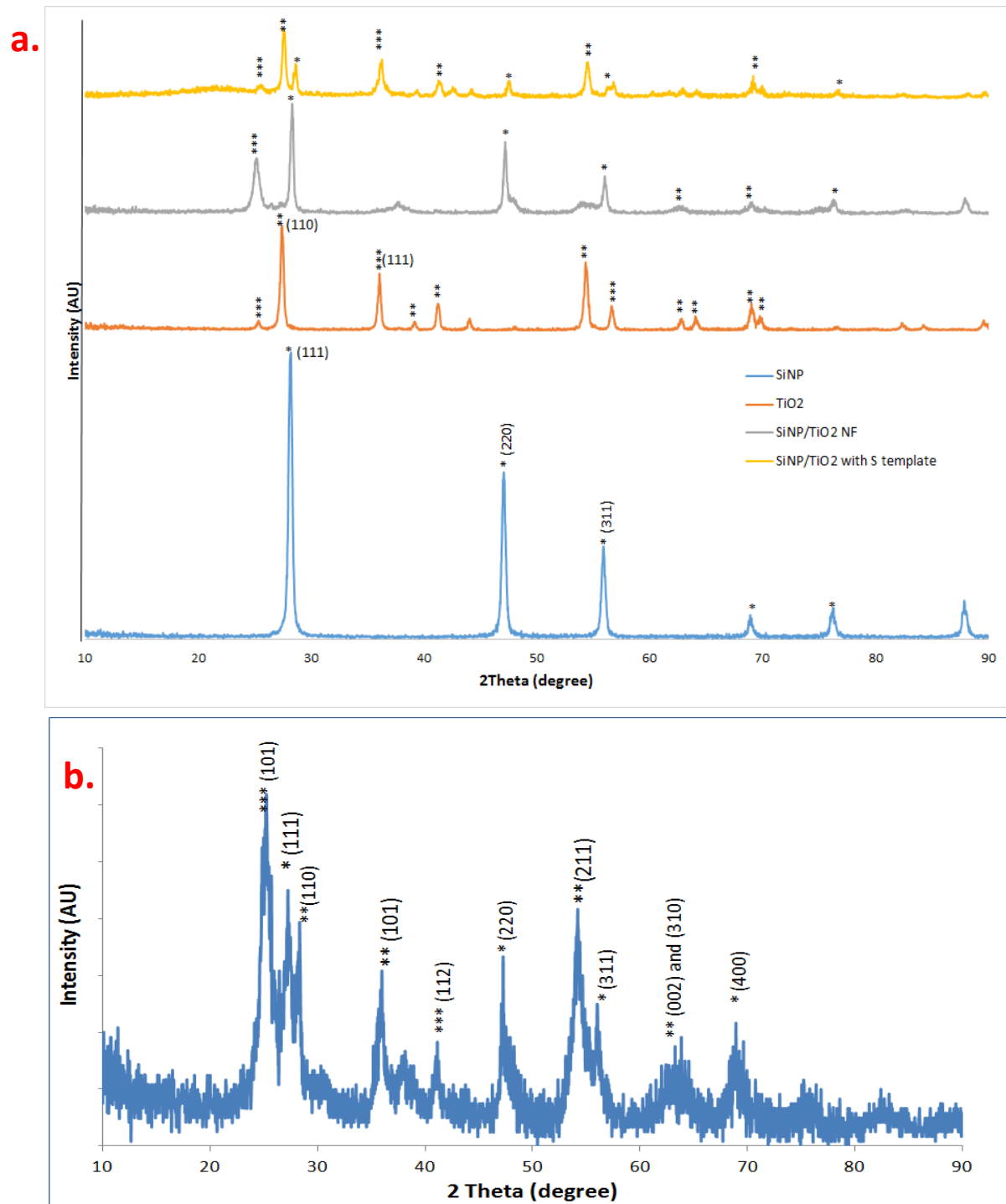


Figure 12: Powder XRD patterns for a) non-carbonized composite nanofibers and b) carbonized SiNP/C/TiO₂ NF with S as a template. Note: * Cubic Silicon, ** Rutile TiO₂ *** Anatase TiO₂[35]

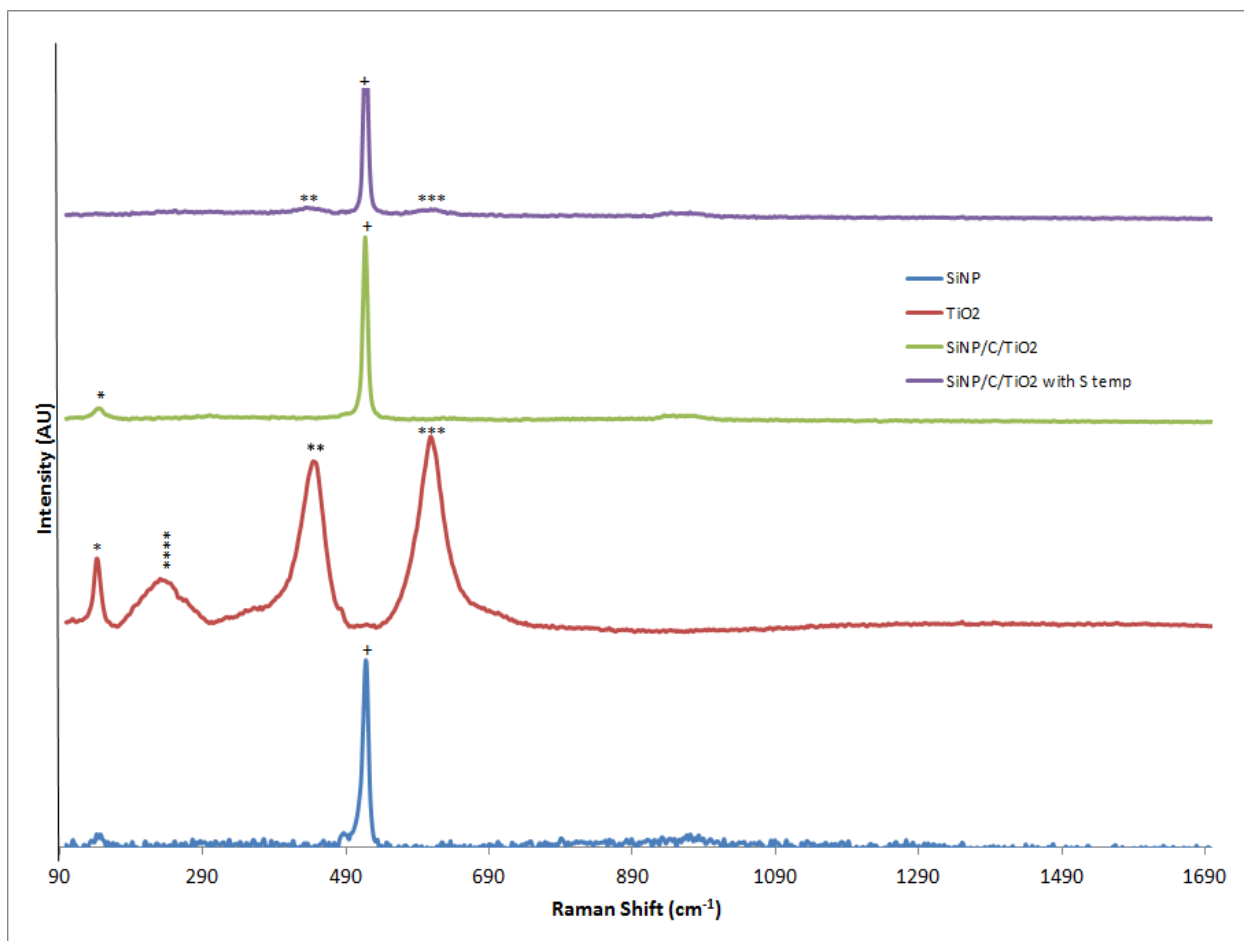
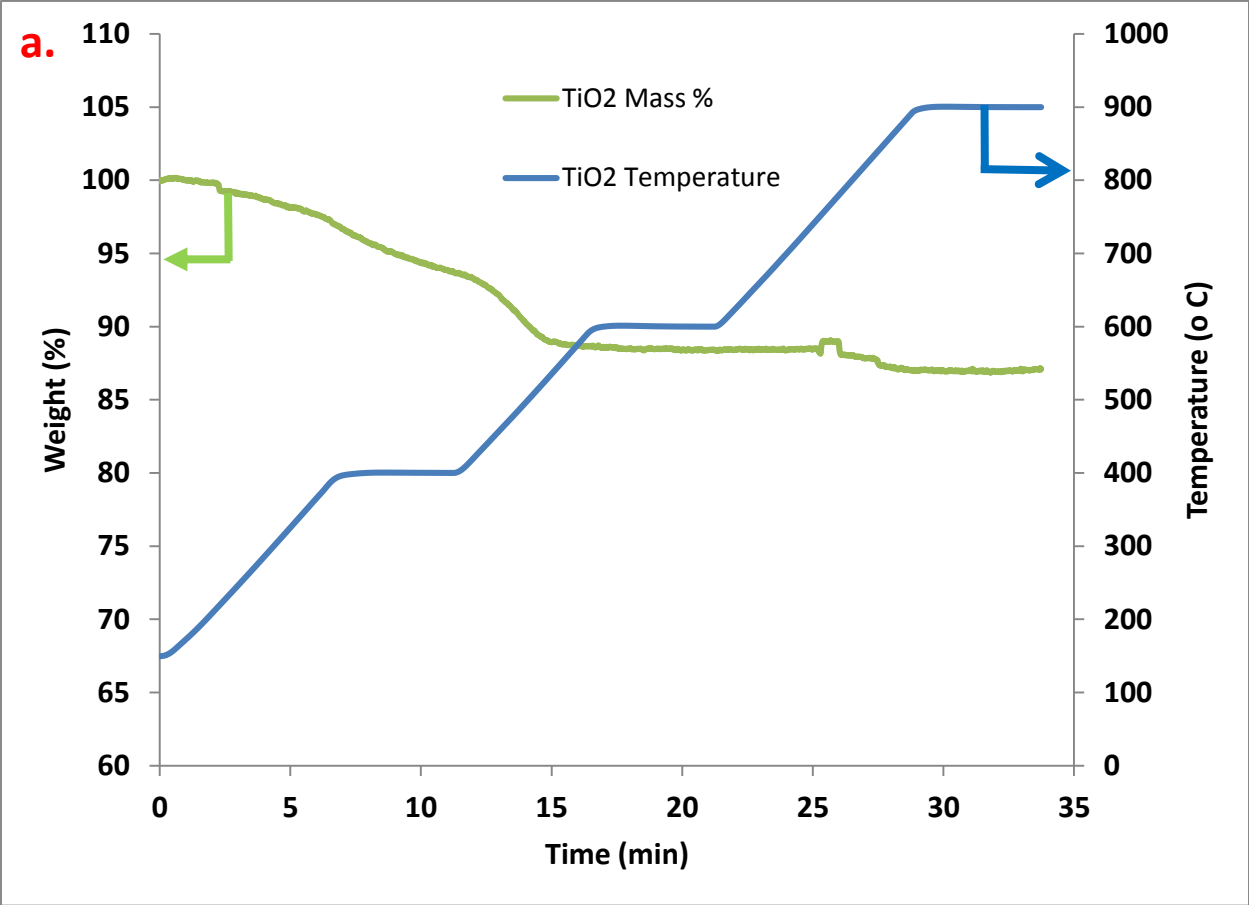
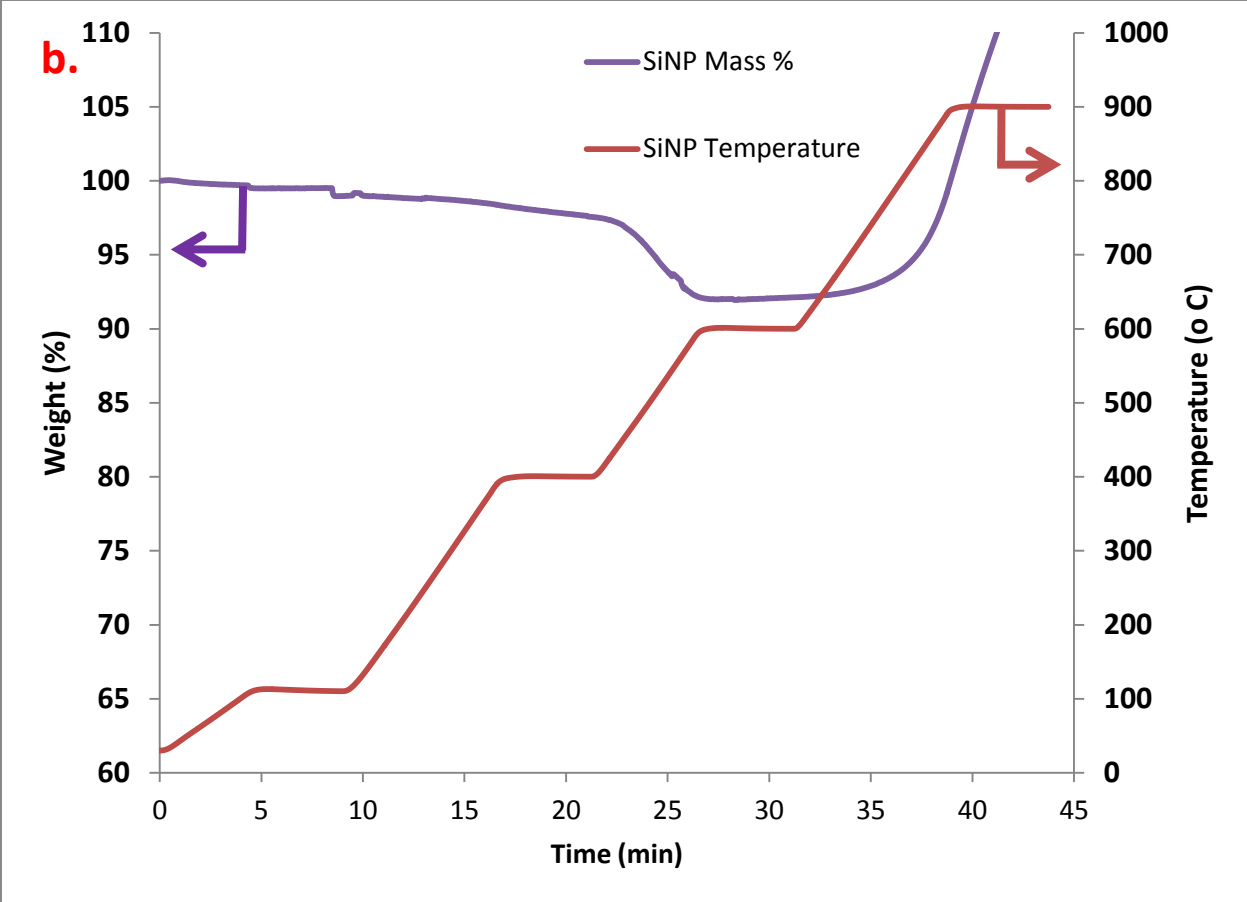
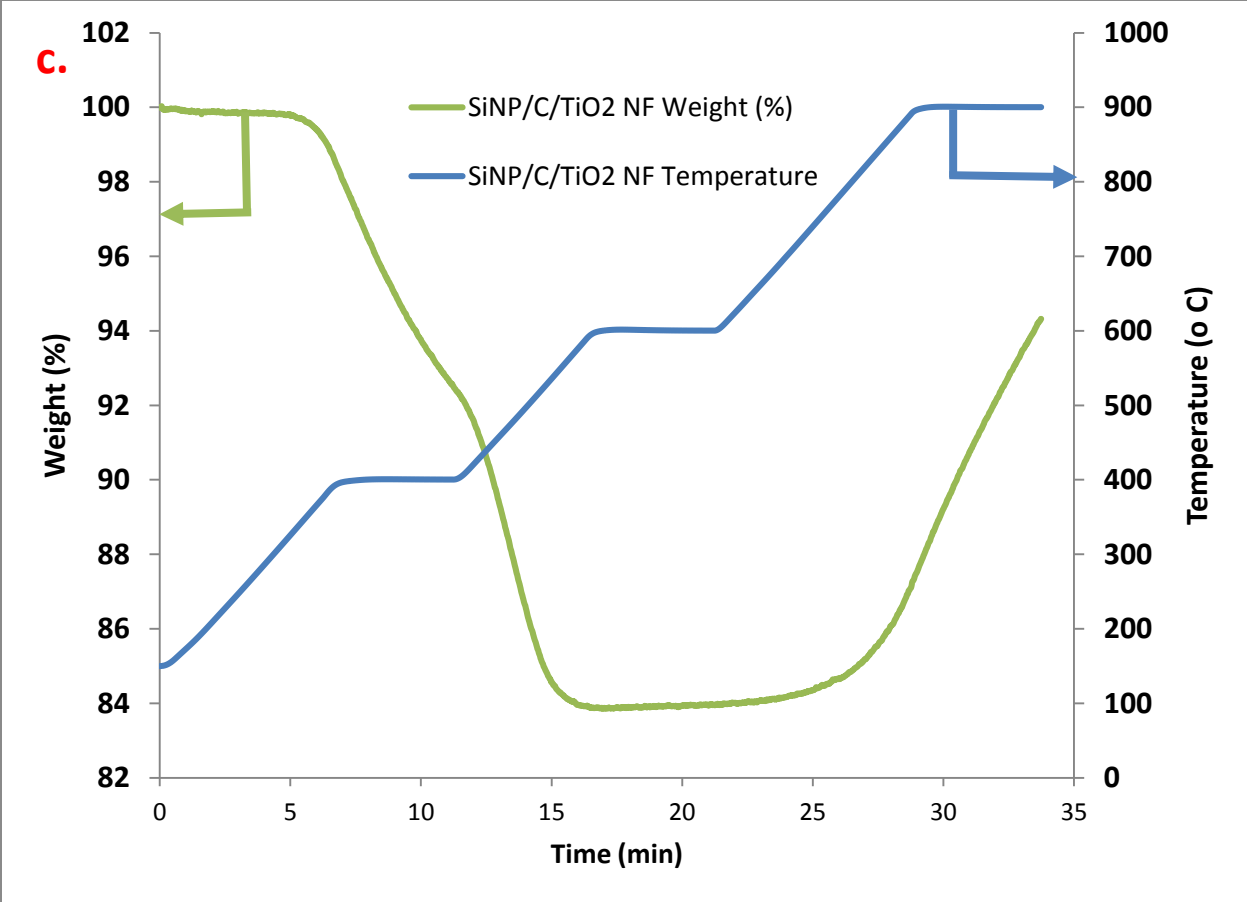
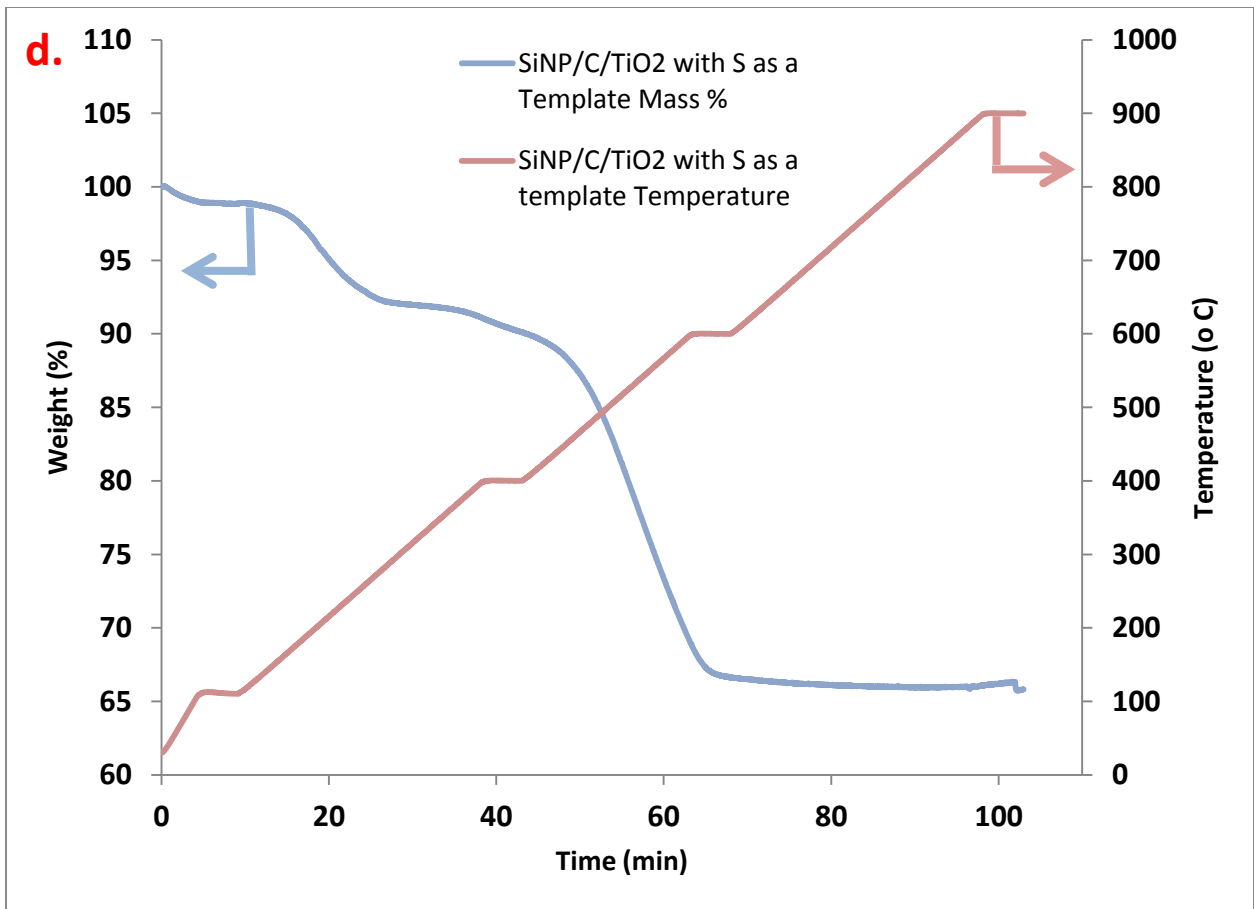


Figure 13: Raman spectrum and characterization of the carbonized NFs. Note: + Cubic Silicon (TO), * B_{1g} Rutile TiO_2 , ** E_g Rutile TiO_2 , *** A_{1g} Rutile TiO_2 , and **** Multi-photon process Rutile TiO_2 [35]. Due to the intensity of the cubic Si peak, the Rutile TiO_2 peaks are overshadowed.









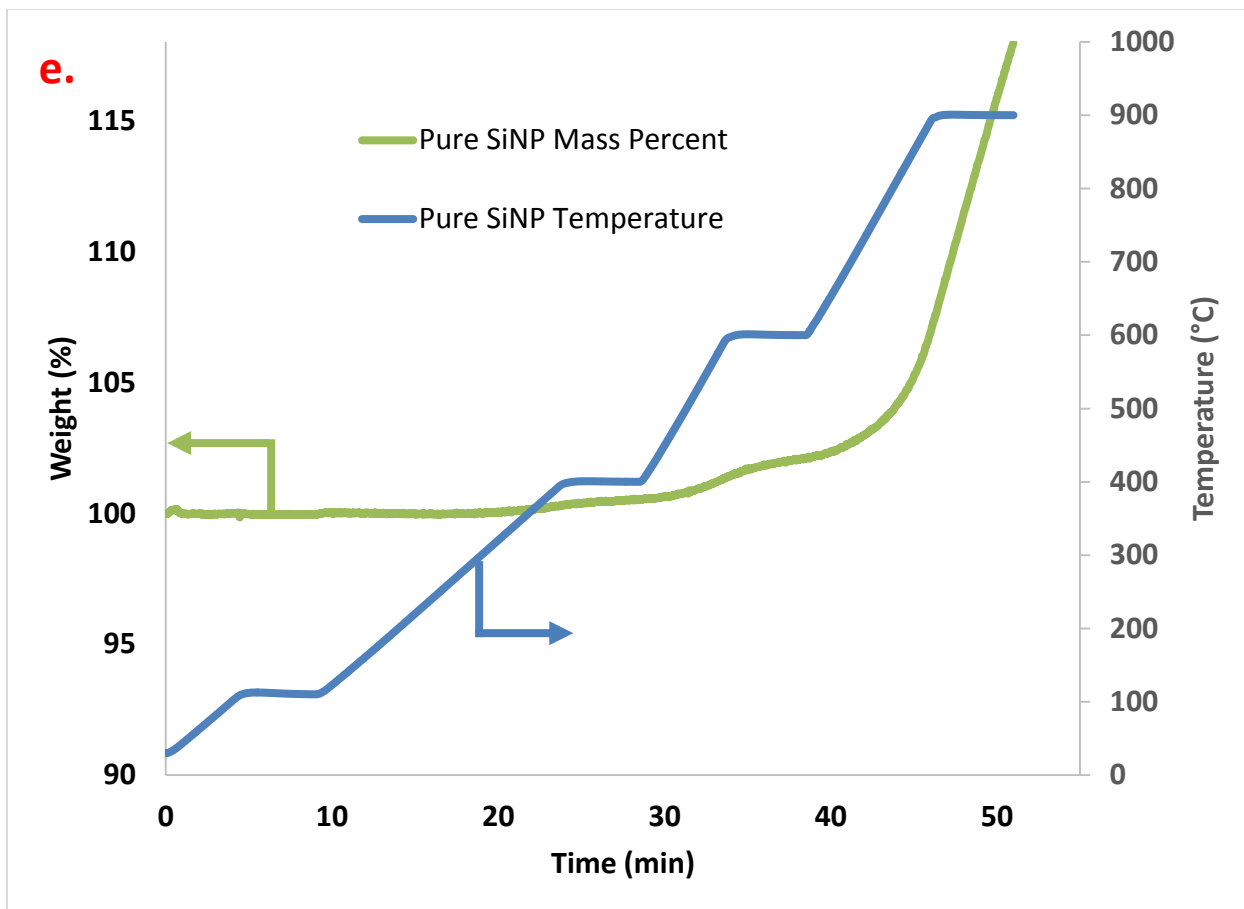
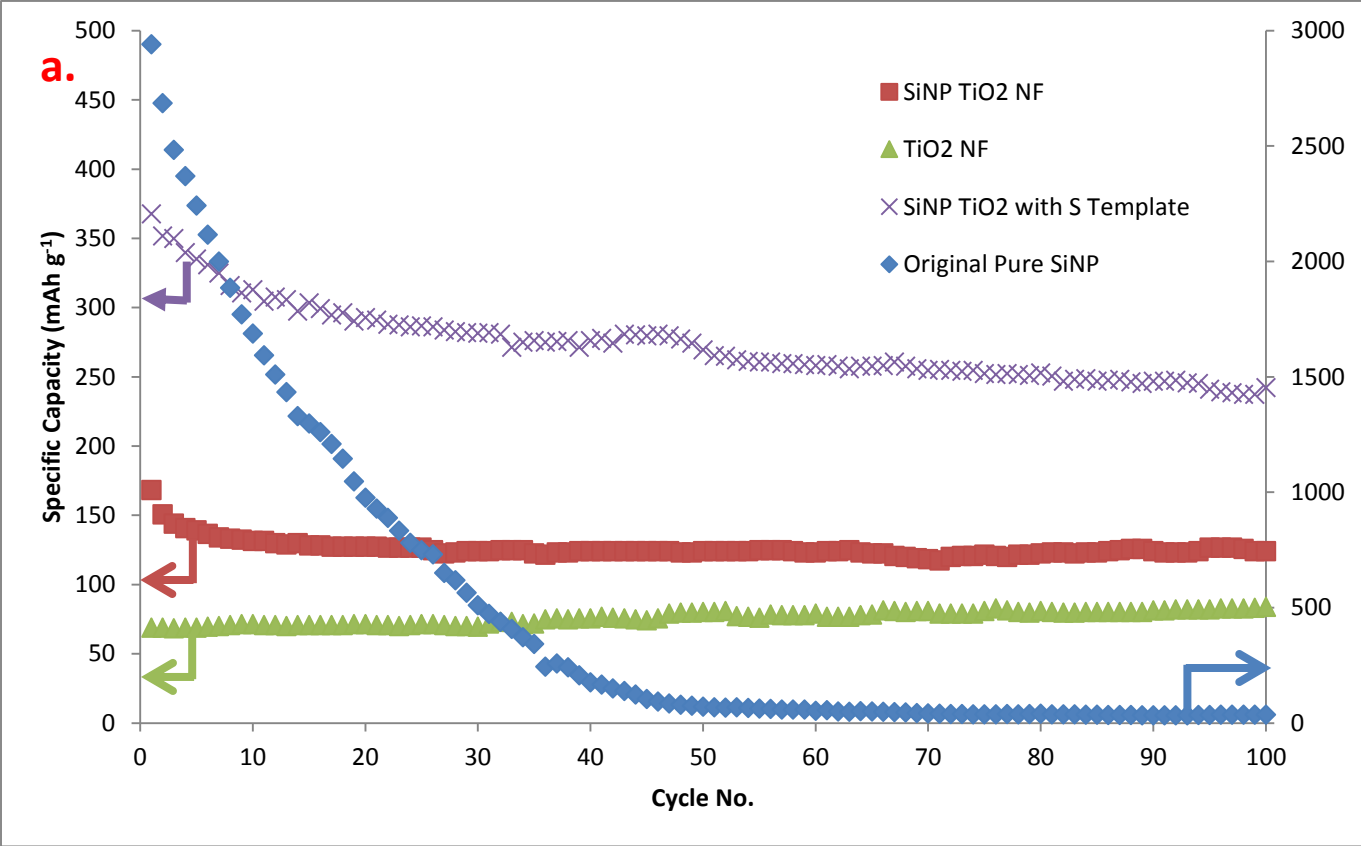


Figure 14: TGA data of carbonized a) TiO₂ NF, b) SiNP, c) SiNP/C/TiO₂ NF, d) SiNP/C/TiO₂ with S template, and e) original pure SiNP. [35]



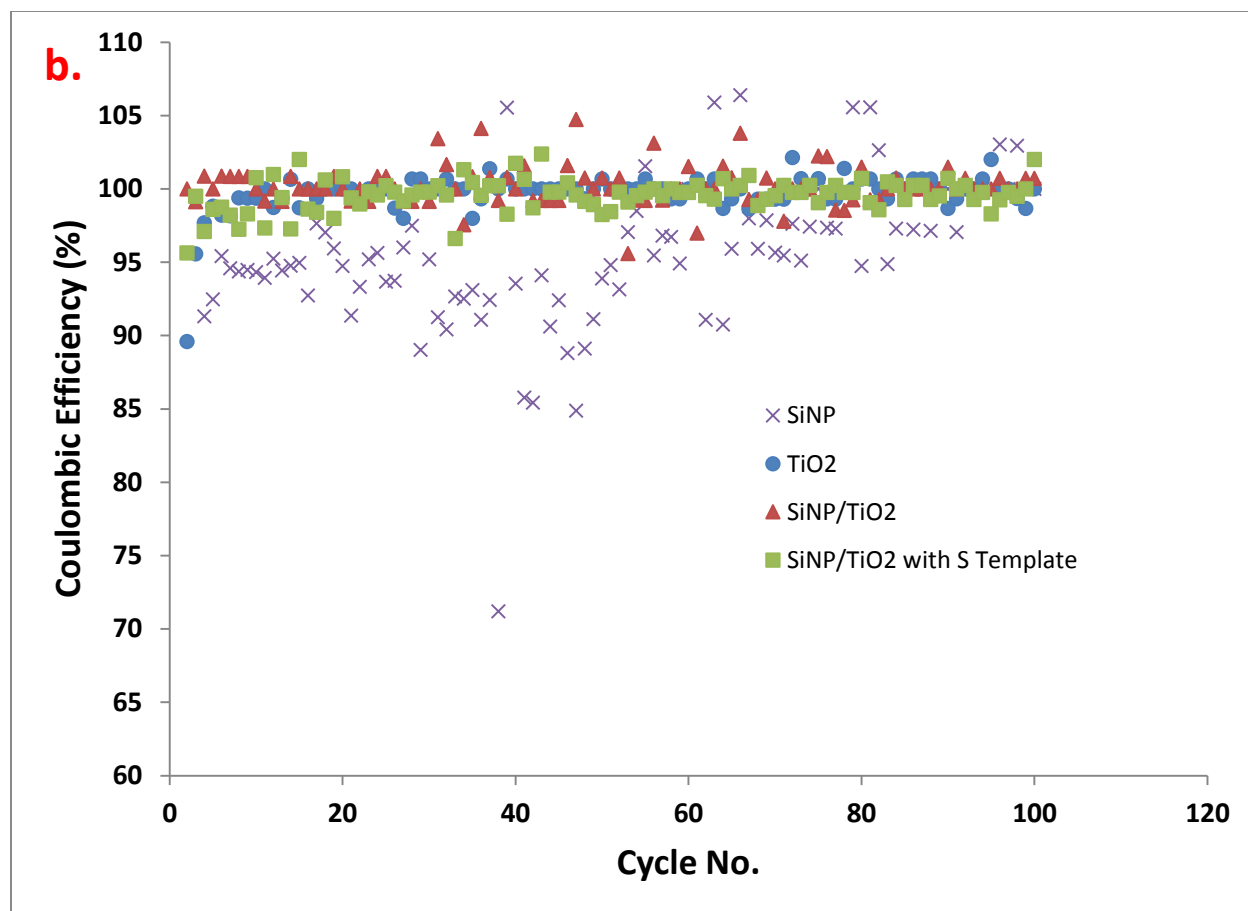


Figure 15: a) Cycling performance and b) coulombic efficiency of non-carbonized samples.

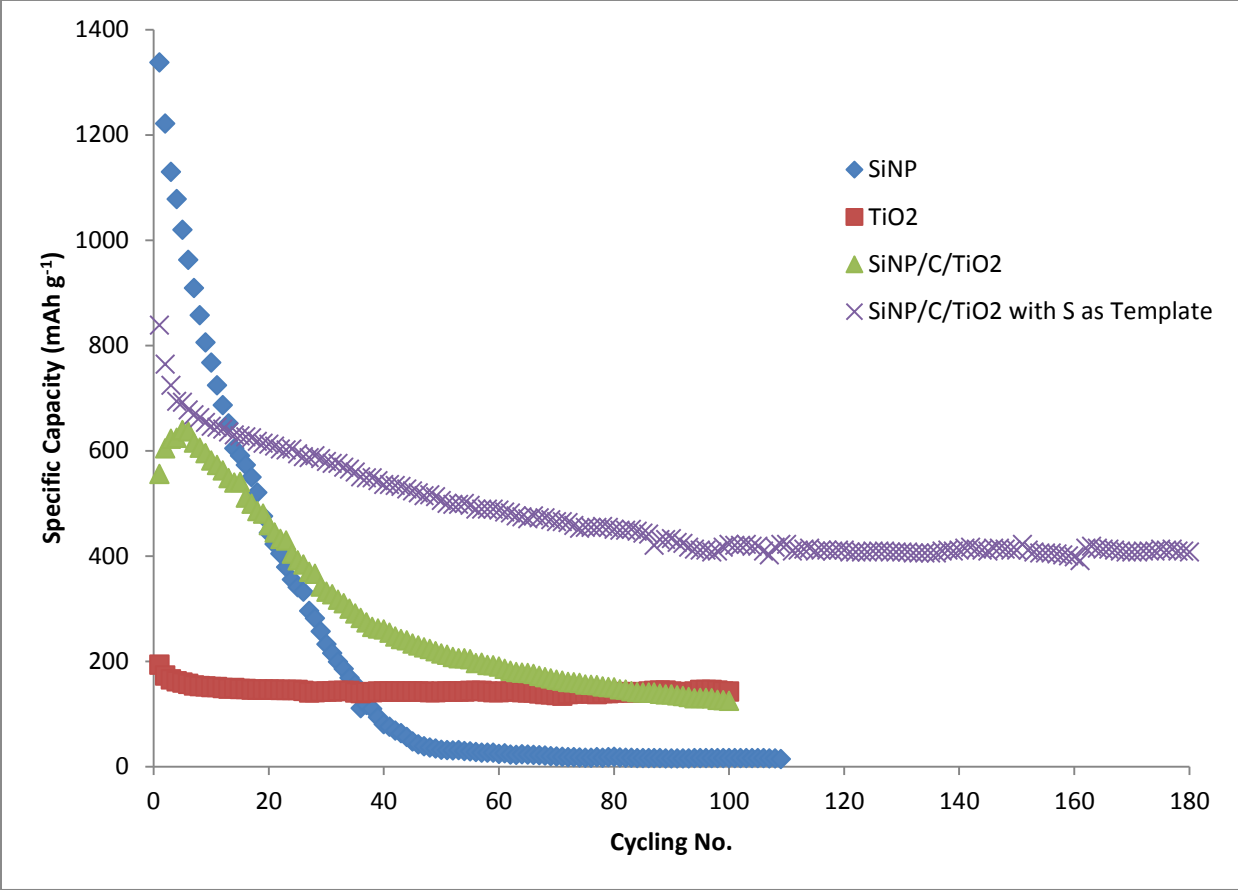


Figure 16: Specific Capacity of carbonized composite nanofibers[35]

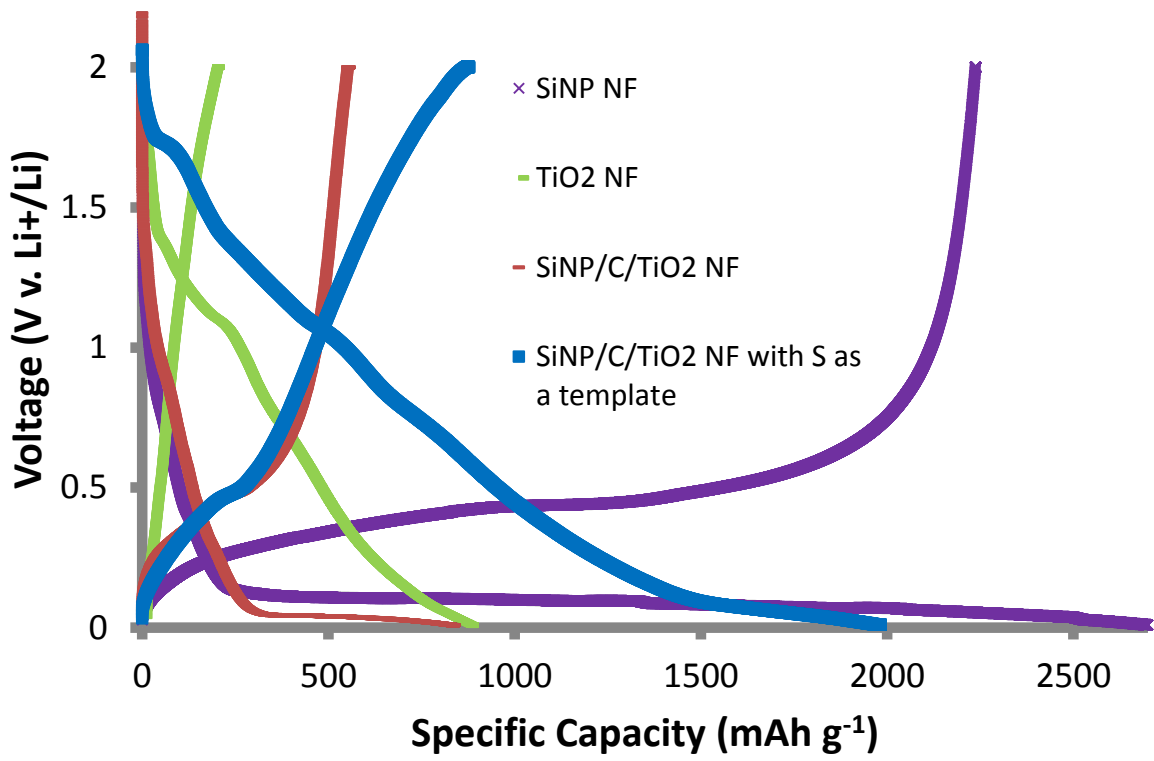


Figure 17: Voltage profile of carbonized composite nanofibers[35]

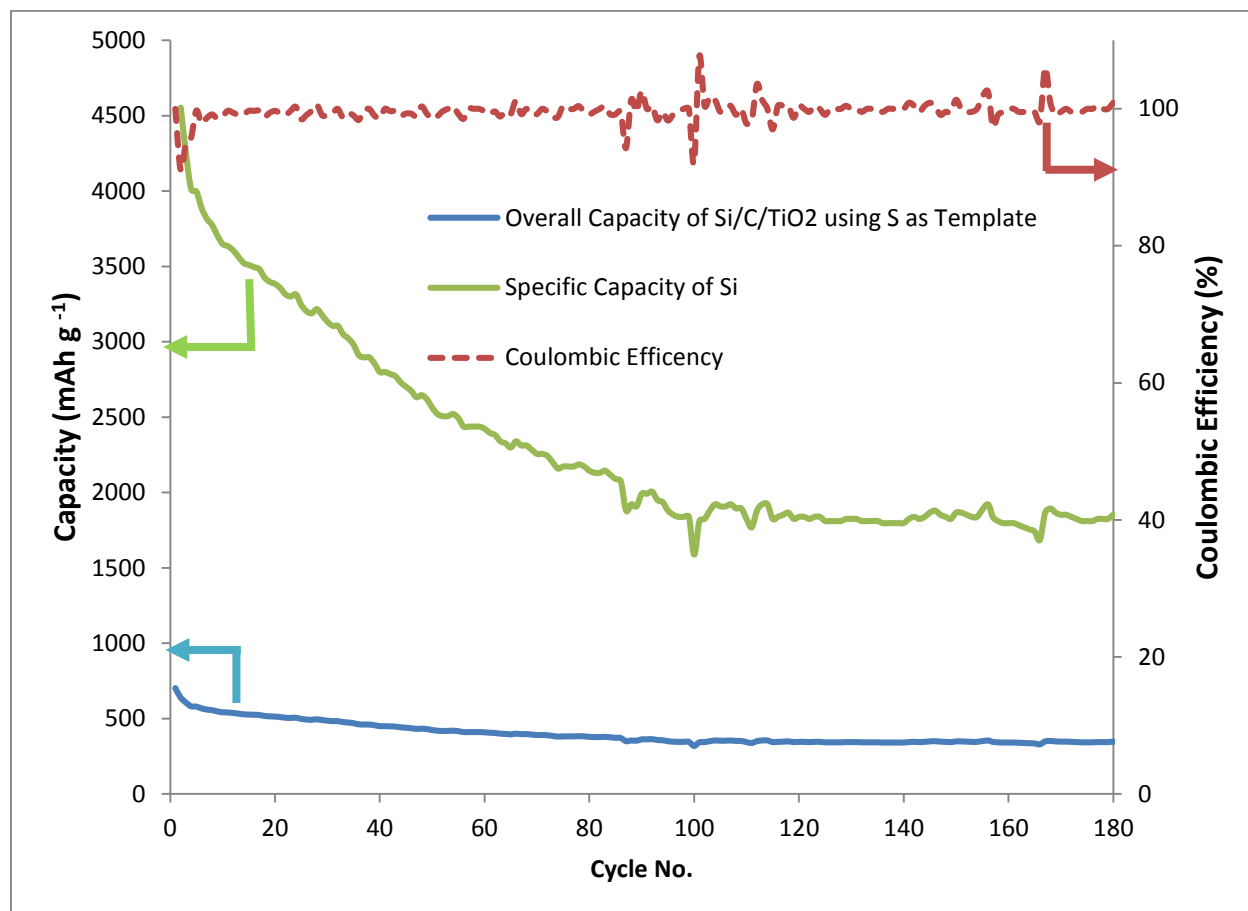


Figure 18: Coulombic efficiency, overall specific capacity, and specific capacity of SiNP contribution of the carbonized SiNP/C/TiO₂ NF with S as a template[35]

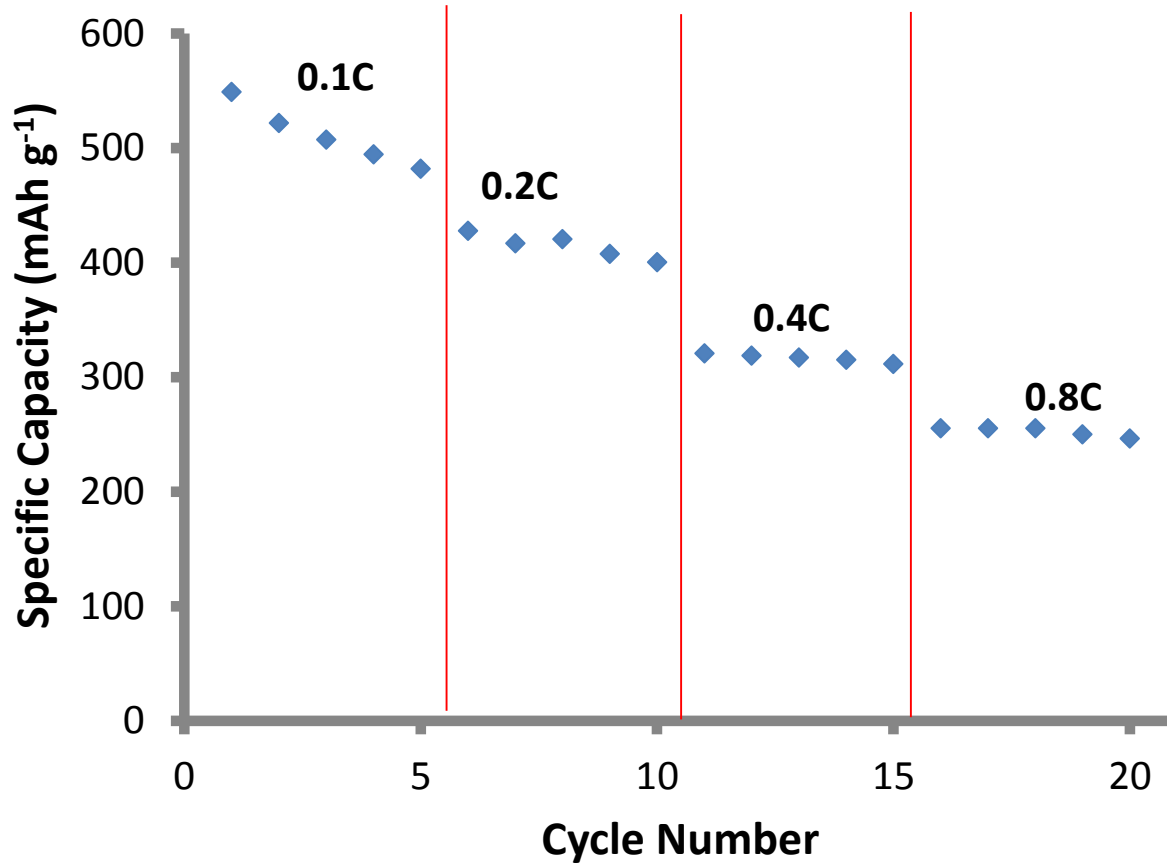


Figure 19: C-rate performance of carbonized SiNP/C/TiO₂ NF with S as a template[35]

Tables

Material	TiO₂	SiNP/TiO₂	SiNP/TiO₂ w/ S Template
Surface Area (m² g⁻¹)	3.85	11.39	17.24

Table 1: The surface area measured using BET Analysis of noncarbonized samples

Material	SiNP	TiO₂	SiNP/C/TiO₂	SiNP/C/TiO₂ w/ S Template
Surface Area (m² g⁻¹)	25	58	77	378

Table 2: The surface area found using BET Analysis of carbonized samples.

References

1. Goodenough, J.B. and K.S. Park, *The Li-Ion Rechargeable Battery: A Perspective*. Journal of the American Chemical Society, 2013. **135**(4): p. 1167-1176. DOI: 10.1021/ja30914381
2. Delair R., W.M., Burke A. *Batteries: Types and History A Condensed History of Batteries*. Edison Tech Center, 2010. Available from: <http://www.edisontechcenter.org/batteries.html>. (accessed November 13, 2014).
3. American Chemical Society National Historic Chemical Landmarks. *The Columbia Dry Cell Battery*. 2005. Available from: <http://www.acs.org/content/acs/en/education/whatischemistry/landmarks/drycellbattery.html>. (accessed November 13, 2014).
4. *Technical Assessment Report: A Technical Assessment of High Energy Batteries for Light-Duty Electric Vehicles*. Global Climate and Energy Project. Stanford University, 2006. Available from: http://gcep.stanford.edu/pdfs/assessments/ev_battery_assessment.pdf. (accessed November 13, 2014).
5. Tarascon, J.M. and M. Armand, *Issues and challenges facing rechargeable lithium batteries*. Nature, 2001. **414**(6861): p. 359-367. DOI: 10.1038/35104644.
6. Moshtev, R. and B. Johnson, *State of the art of commercial Li ion batteries*. Journal of Power Sources, 2000. **91**(2): p. 86-91. DOI: 10.1016/S0378-7753(00)00458-4.
7. Simon, G.K., et al., *Silicon-coated carbon nanofiber hierarchical nanostructures for improved lithium-ion battery anodes*. Journal of Power Sources, 2011. **196**(23): p. 10254-10257. DOI: 10.1016/j.jpowsour.2011.08.058.
8. Hwang, T.H., et al., *Electrospun Core-Shell Fibers for Robust Silicon Nanoparticle-Based Lithium Ion Battery Anodes*. Nano Letters, 2012. **12**(2): p. 802-807. DOI: 10.1021/nl203817r.
9. Tian, Q., et al., *Encapsulation of SnO₂ nanoparticles into hollow TiO₂ nanowires as high performance anode materials for lithium ion batteries*. Journal of Power Sources, 2014. **253**: p. 9-16. DOI: 10.1016/j.jpowsour.2013.12.049.
10. Amine, K., et al., *Nanostructured Anode Material for High-Power Battery System in Electric Vehicles*. Advanced Materials, 2010. **22**(28): p. 3052-3057. DOI: 10.1002/adma.201000441.
11. *Overview: Lithium Ion Batteries*. 2007, Panasonic. p. 26-28. Available from: <http://industrial.panasonic.com/lccs/www-data/pdf/ACA4000/ACA4000PE3.pdf>. (accessed February 14, 2014)
12. Landi, B.J., et al., *Carbon nanotubes for lithium ion batteries*. Energy & Environmental Science, 2009. **2**(6): p. 638-654. DOI: 10.1039/b904116h.
13. Jeong, G., et al., *Core-Shell Structured Silicon Nanoparticles@TiO₂-x/Carbon Mesoporous Microfiber Composite as a Safe and High-Performance Lithium-Ion Battery Anode*. ACS Nano, 2014. **8**(3): p. 2977-2985. DOI: 10.1021/nm500278q.
14. Nie, M.Y., et al., *Silicon Solid Electrolyte Interphase (SEI) of Lithium Ion Battery Characterized by Microscopy and Spectroscopy*. Journal of Physical Chemistry C, 2013. **117**(26): p. 13403-13412. DOI: 10.1021/jp404155yl.
15. Liu, X.R., et al., *Single Nanowire Electrode Electrochemistry of Silicon Anode by in Situ Atomic Force Microscopy: Solid Electrolyte Interphase Growth and Mechanical Properties*. ACS Applied Materials & Interfaces, 2014. **6**(22): p. 20317-20323. DOI: 10.1021/am404847s.
16. Tikhonov, K. and V.R. Koch. *Li-ion Battery Electrolytes Designed for a Wide Temperature Range*. Covalent Associates, Inc. Available from: <http://www.covalentassociates.com/Li-ion%20Battery%20Electrolytes%20Designed%20For%20a%20Wide%20Temperature%20Range.pdf>. (accessed January 12, 2015).
17. Wang, Y. and W.H. Zhong, *Development of Electrolytes towards Achieving Safe and High-Performance Energy-Storage Devices: A Review*. ChemElectroChem, 2015. **2**(1): p. 22-36. DOI: 10.1002/celec.201402277.

18. Jeong, M., et al., *Effect of electrolyte on cycle performances of the electrodeposited Sn-O-C composite anode of lithium secondary batteries*. Journal of Power Sources, 2015. **275**: p. 525-530. DOI: 10.1016/j.jpowsour.2014.11.008.
19. Karmakar, A. and A. Ghosh, *Structure and ionic conductivity of ionic liquid embedded PEO-LiCF₃SO₃ polymer electrolyte*. Aip Advances, 2014. **4**(8). DOI: 10.1063/1.4892855.
20. Kim, D.W., et al., *Gel-coated membranes for lithium-ion polymer batteries*. Solid State Ionics, 2000. **138**(1-2): p. 41-49. DOI: 10.1016/S0167-2738(00)00763-3.
21. Song, J.Y., Y.Y. Wang, and C.C. Wan, *Review of gel-type polymer electrolytes for lithium-ion batteries*. Journal of Power Sources, 1999. **77**(2): p. 183-197. DOI: 10.1016/S0378-7753(98)00193-1.
22. Wang, Y., J. Travas-Sejdic, and R. Steiner, *Polymer gel electrolyte supported with microporous polyolefin membranes for lithium ion polymer battery*. Solid State Ionics, 2002. **148**(3-4): p. 443-449. DOI: 10.1016/S0167-2738(02)00085-1.
23. Pu, W.H., et al., *Preparation of PVDF-HFP microporous membrane for Li-ion batteries by phase inversion*. Journal of Membrane Science, 2006. **272**(1-2): p. 11-14. DOI: 10.1016/j.jpowsour.2009.02.053.
24. Choi, Y.J., et al., *Effects of carbon coating on the electrochemical properties of sulfur cathode for lithium/sulfur cell*. Journal of Power Sources, 2008. **184**(2): p. 548-552. DOI: 10.1016/j.jpowsour.2009.02.053.
25. He, G., et al., *Bimodal Mesoporous Carbon Nanofibers with High Porosity: Freestanding and Embedded in Membranes for Lithium-Sulfur Batteries*. Chemistry of Materials, 2014. **26**(13): p. 3879-3886. DOI: 10.1021/cm403740r.
26. Kennedy, T., et al., *High-Performance Germanium Nanowire-Based Lithium-Ion Battery Anodes Extending over 1000 Cycles Through in Situ Formation of a Continuous Porous Network*. Nano Letters, 2014. **14**(2): p. 716-723. DOI: 10.1021/nl403979s.
27. Yuan, F.W. and H.Y. Tuan, *Scalable Solution-Grown High-Germanium-Nanoparticle-Loading Graphene Nanocomposites as High-Performance Lithium-Ion Battery Electrodes: An Example of a Graphene-Based Platform toward Practical Full-Cell Applications*. Chemistry of Materials, 2014. **26**(6): p. 2172-2179. DOI: 10.1021/cm4002016.
28. Veeraraghavan, B., et al., *Study of Sn-coated graphite as anode material for secondary lithium-ion batteries*. Journal of the Electrochemical Society, 2002. **149**(6): p. A675-A681. DOI: 10.1149/1.1470653.
29. Tran, T., et al., *Electrospun SnO₂ and TiO₂ Composite Nanofibers for Lithium Ion Batteries*. Electrochimica Acta, 2014. **117**: p. 68-75. DOI: 10.1016/j.electacta.2013.11.101.
30. Chen, S., et al., *Microwave hydrothermal synthesis of high performance tin-graphene nanocomposites for lithium ion batteries*. Journal of Power Sources, 2012. **216**: p. 22-27. DOI: 10.1016/j.jpowsour.2012.05.051.
31. Wu, H. and Y. Cui, *Designing nanostructured Si anodes for high energy lithium ion batteries*. Nano Today, 2012. **7**(5): p. 414-429. DOI: 10.1016/j.nantod.2012.08.004.
32. Wu, Q., et al., *Electrospun silicon/carbon/titanium oxide composite nanofibers for lithium ion batteries*. Journal of Power Sources, 2014. **258**: p. 39-45. DOI: 10.1016/j.jpowsour.2014.02.047.
33. Zhang, S.S., et al., *Understanding solid electrolyte interface film formation on graphite electrodes*. Electrochemical and Solid State Letters, 2001. **4**(12): p. A206-A208. DOI: 10.1149/1.1414946.
34. Yi, R., et al., *Influence of Silicon Nanoscale Building Blocks Size and Carbon Coating on the Performance of Micro-Sized Si-C Composite Li-Ion Anodes*. Advanced Energy Materials, 2013. **3**(11): p. 1507-1515. DOI: 10.1002/aenm.201300496.
35. McCormac, K., et al., *Preparation of porous Si and TiO₂ nanofibres using a sulphur-templating method for lithium storage*. 2015: p. 1-5. DOI: 10.1002/psa.201431834.

36. Wang, C., et al., *Self-healing chemistry enables the stable operation of silicon microparticle anodes for high-energy lithium-ion batteries*. *Nature chemistry*, 2013. **5**(12): p. 1042-8. DOI: 10.1038/NCHEM.1802.
37. Wu, M.Y., et al., *In Situ Formed Si Nanoparticle Network with Micron-Sized Si Particles for Lithium-Ion Battery Anodes*. *Nano Letters*, 2013. **13**(11): p. 5397-5402. DOI: 10.1021/nl402953h.
38. Si, Q., et al., *Improvement of cyclic behavior of a ball-milled SiO and carbon nanofiber composite anode for lithium-ion batteries*. *Journal of Power Sources*, 2011. **196**(22): p. 9774-9779. DOI: 10.1016/j.jpowsour.2011.08.005.
39. Luais, E., et al., *Mesoporous silicon negative electrode for thin film lithium-ion microbatteries*. *Journal of Power Sources*, 2015. **274**: p. 693-700. DOI: 10.1016/j.jpowsour.2014.10.084.
40. Jing, S., et al., *Directly grown Si nanowire arrays on Cu foam with a coral-like surface for lithium-ion batteries*. *Nanoscale*, 2014. **6**(23): p. 14441-14445. DOI: 10.1039/c4n405469e.
41. Si, Q., et al., *High performance Si/C@CNF composite anode for solid-polymer lithium-ion batteries*. *Journal of Power Sources*, 2011. **196**(16): p. 6982-6986. DOI: 10.1016/j.jpowsour.2010.10.091
42. Su, X., et al., *Silicon-Based Nanomaterials for Lithium-Ion Batteries: A Review*. *Advanced Energy Materials*, 2014. **4**(1): p. 23. DOI: 10.1002/aenm.201300882.
43. Su, X., et al., *Advanced titania nanostructures and composites for lithium ion battery*. *Journal of Materials Science*, 2012. **47**(6): p. 2519-2534. DOI: 10.1007/s10853-011-5974-x.
44. Dambournet, D., I. Belharouak, and K. Amine, *Tailored Preparation Methods of TiO₂ Anatase, Rutile, Brookite: Mechanism of Formation and Electrochemical Properties*. *Chemistry of Materials*, 2010. **22**(3): p. 1173-1179. DOI: 10.1021/cm902613h
45. Hu, M., et al., *Direct Carbonization of Al-Based Porous Coordination Polymer for Synthesis of Nanoporous Carbon*. *Journal of the American Chemical Society*, 2012. **134**(6): p. 2864-2867. DOI: 10.1021/ja208940u.
46. Sponchia, G., et al., *Mesoporous silica nanoparticles with tunable pore size for tailored gold nanoparticles*. *Journal of Nanoparticle Research*, 2014. **16**(2). DOI:10.1007/s11051-014-2245-1.
47. Kurc, B., *Gel electrolytes based on poly(acrylonitrile)/sulpholane with hybrid TiO₂/SiO₂ filler for advanced lithium polymer batteries*. *Electrochimica Acta*, 2014. **125**: p. 415-420. DOI: 10.1016/j.electacta.2014.01.117.
48. Hu, H., et al., *Photodeposition of Ag₂S on TiO₂ nanorod arrays for quantum dot-sensitized solar cells*. *Nanoscale Research Letters*, 2013. **8**(10). DOI: 10.1186/1556-276X-8-10
49. Feng, X., et al., *Facile approach to an advanced nanoporous silicon/carbon composite anode material for lithium ion batteries*. *Rsc Advances*, 2012. **2**(13): p. 5701-5706. DOI: 10.1039/c2ra20107k.
50. Hatchard, T.D. and J.R. Dahn, *In situ XRD and electrochemical study of the reaction of lithium with amorphous silicon*. *Journal of the Electrochemical Society*, 2004. **151**(6): p. A838-A842. DOI: 10.1149/1.1739217.
51. Hu, A., et al., *Two novel hierarchical homogeneous nanoarchitectures of TiO₂ nanorods branched and P25-coated TiO₂ nanotube arrays and their photocurrent performances*. *Nanoscale Research Letters*, 2011. **6**(91). DOI: 10.1186/1556-276X-6-91.
52. Lu, S.W., et al., *Phase sensitivity of Raman spectroscopy analysis of CVD titania thin films*. *Journal of Materials Science*, 2009. **44**(2): p. 541-544. DOI: 10.1007/s10853-008-3086-z.
53. Quiroga-Gonzalez, E., et al., *Pore size modulation in electrochemically etched macroporous p-type silicon monitored by FFT impedance spectroscopy and Raman scattering*. *Physical Chemistry Chemical Physics*, 2014. **16**(1): p. 255-263. DOI: 10.1039/c3cp53600a.
54. Tuinstra, F. and J.L. Koenig, *Raman Spectrum of Graphite*. *The Journal of Chemical Physics*, 1970. **53**(3): p. 1126-1130. DOI: 10.1063/1.1674108.
55. Fang, M., et al., *Covalent polymer functionalization of graphene nanosheets and mechanical properties of composites*. *Journal of Materials Chemistry*, 2009. **19**(38): p. 7098-7105. DOI: 10.1039/b908220d.

56. Ben Hlel, D., et al., *Analysis of optical and thermal properties of thermally oxidized mesoporous silicon layers*. *Microporous and Mesoporous Materials*, 2015. **204**: p. 137-142. DOI: 10.1016/j.micromeso.2014.11.016.
57. Reddy, M.A., et al., *Room temperature synthesis and Li insertion into nanocrystalline rutile TiO₂*. *Electrochemistry Communications*, 2006. **8**(8): p. 1299-1303. DOI: 10.1016/j.elecom.2006.05.021.
58. Pfanzelt, M., et al., *TiO₂ rutile—An alternative anode material for safe lithium-ion batteries*. *Journal of Power Sources*, 2011. **196**(16): p. 6815-6821. DOI: 10.1016/j.jpowsour.2010.09.109.

Addendum: (Silicon Micron Powder and Titanium Dioxide Composite Nanofibers for Lithium Ion Batteries)

1. Experimental

1.1 Titanium Dioxide Nanofiber (TiO₂)

The fabrication of titanium dioxide nanofibers started with the preparation of 10% wt/v polymeric solution by mixing ~1 gram of polyvinylpyrrolidone [(PVP), Sigma Aldrich, MW: 1.3M] with 10 mL of ethanol. In a separate container, ~3 grams of titanium isopropoxide [(TiIP), Agros Organics 98%] with 5 mL of ethanol (Pharmco Inc, 99.9%) and 3 mL of Acetic Acid (Agros Organics, 99%). These solutions were vortexed separately for ~30 minutes to insure a thorough mixture. Then they were added together and vortexed again for another 5 minutes. This mixture was then sonicated for 20 minutes.

1.2 Silicon Micron Powder Titanium Dioxide (Si/TiO₂) Nanofibers

The fabrication of titanium dioxide/ silicon (Alfa, 1-5 microns) nanofibers began with the mixing of ~3 grams TiIP, 1 gram of silicon powder, 3 mL Acetic Acid and 5 mL of ethanol. In another separate container, 1 gram of PVP and 10 mL of ethanol were mixed. Both mixtures were vortexed for ~30 minutes then combined and vortexed again for another 5 minutes. The sol-gel was then sonicated for 20 minutes.

1.3 Silicon/TiO₂ Nanofiber with S as a template (Si/TiO₂ with S as a template)

For this fabrication, 2.5 g sulfur (Agros Organics, 99.8% sublimed) and 1 g silicon powder were ground together by mortar and pestle. This combination was then mixed with 3 g TiIP, 5 mL of ethanol, and 3 mL of acetic acid. In another vial, 10 mL ethanol and 1 gram of PVP were

combined. Both vials were then vortexed for 30 minutes separately. Then these solutions were combined and vortexed for another 5 minutes. The sol-gel was then sonicated for 20 minutes.

1.4 Electrospinning and Post-treatment

Once the solution of the intended nanofiber was completed, it was used for electrospinning. A syringe of 14.5 mm in inner diameter was placed 12-15 cm from the grounding electrode and the solution was electrospun at a rate of 5 mL/hr at 25kV (SyringePump, Model NE300, 12VDC, 0.75A). Once all the sol-gel has been electrospun, the fibers were left overnight for further gelling and then put into an oven at ~ 565°C overnight.

1.5 Electrode Preparation

The next step was to make a slurry using the different composite nanofibers of TiO₂ and silicon micron powder. The slurry contained 80% w/w of nanofibers or composite nanofiber, 10% carbon black [MTI Corporation], and 10% polyvinylidene fluoride (PVDF) [MTI Corporation] binder in N-methyl-2-pyrrolidone [(NMP), Sigma Aldrich, >99.5%]. The slurry was sonicated for 2 hours to make sure the particles and NFs were well dispersed. Copper disks were used as a current collector for the LIB. The slurry was then coated on the 15 mm diameter Cu disk to make the electrode. It was important to make sure the entire Cu foil was coated as evenly as possible. The electrodes were placed in a vacuum and heated at 100 °C overnight to remove solvent and any residual moisture.

1.6 Battery Fabrication

In the glove box with well controlled concentration of O₂ and H₂O (< 1ppm), the electrode was assembled into half-cells using lithium metal as the counter electrode. The membrane placed between the active material electrode and counter electrode is made of polyethylene/polypropylene

[MTI Corporation, pore size 20-30nm]. Due to the softness of Li metal, a steel spacer [MTI Corporation] was placed on top of the Li counter electrode. Similarly, 1 M LiPF₆ dissolved in EC/DMC/DEC 1:1:1 in volume (MTI Corporation) was used as the electrolyte. The fabrication process is portrayed in Figure 3 of the thesis. The 2032 coin cell battery was crimped together under 100lbs of force.

2. Characterization of Si micron powder nanofibers

Just like the silicon nanoparticle project, BET, SEM-EDS, powder XRD, and Raman Spectroscopy were used to characterize the nanofibers. BET (Micromeritics ASAP 2020 Surface Area and Porosity Analyzer) data shows that the specific area of pure TiO₂ and TiO₂/Si Powder are 3.85 and 11.39 m²/g, respectively using N₂ as adsorption gas. SEM-EDS (SEM-JEOL SEM model JSM7600F) has been performed on TiO₂ (Figure 1a) and Si/TiO₂ NF with S as a template (Figure 1b). Powdered XRD (Rigaku model MiniFlex 600, $\kappa\alpha=1.54\text{\AA}$ (Cu)) was measured at Armstrong Atlantic State University with the help of Dr. Clifford Padgett (Figure 2). Based on the control peaks of rutile TiO₂ of 2θ at 27.4°, 36.1°, and 54.3°, it can be determined that rutile TiO₂ is present in all samples [44]. TiO₂ in the anatase phase gives maxima at 2θ values of 25.28, 32, 33, 33.50, 48.05 and 55.06 [44]. Based on the peaks of 28.2°, 47.1°, and 55.9°, one can determine that cubic silicon is present in all the samples excluding that of pure TiO₂. The last data classification technique was Raman Spectroscopy shown in Figures 3. The peak at ~141 cm⁻¹ is consistent with the literature reported value of the B_{1g} peak of TiO₂ rutile phase. The peak around 607 cm⁻¹ is consistent with literature reported value of the A_{1g} peak of TiO₂ rutile phase, and the peak ~444 cm⁻¹ is consistent with the literature value of the E_g peak of the TiO₂ rutile phase.[29] Thus based on these 3 peaks the TiO₂ nanofibers are in the rutile phase.

3. Electrochemical Performance

Si/TiO₂ with S as a template was fabricated into a battery and tested using a potentiostat instrument. Si/TiO₂ with S as a template has a capacity of 145 mAh g⁻¹ after the formation cycles (Figure 4). This value is even lower than commercially available graphite-based lithium ion batteries. This battery only retained 22% of its initial capacity after 100 cycles.

4. Conclusion

Due to large volume expansion during lithiation process, the electrode containing micron size silicon degraded quickly due to the pulverization of the electrode, resulting in unstable SEI layers and fast degradation of the battery capacity. More extensive research is needed to address the issue of poor mechanical strength of silicon material at micron-scale.

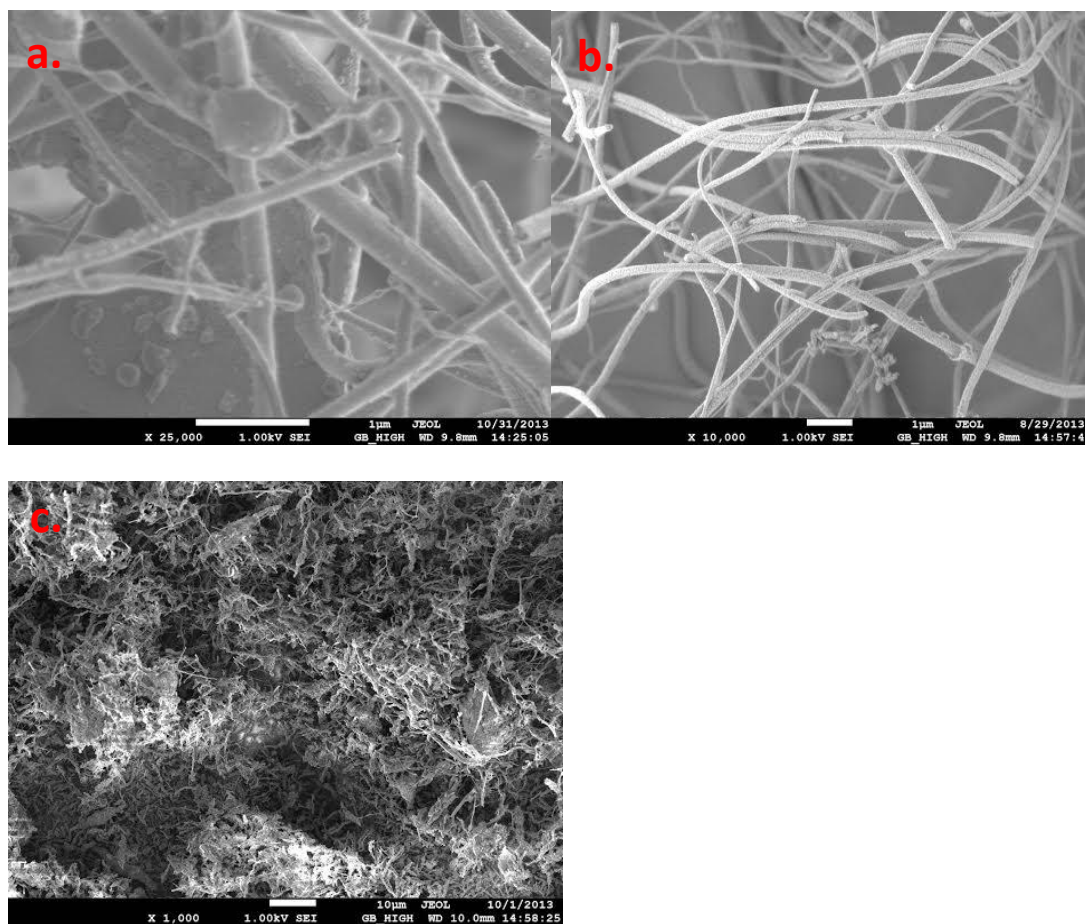


Figure 1: SEM Images of a) TiO_2 , b) Si/TiO_2 , and c) Si/TiO_2 with S as a template NFs.

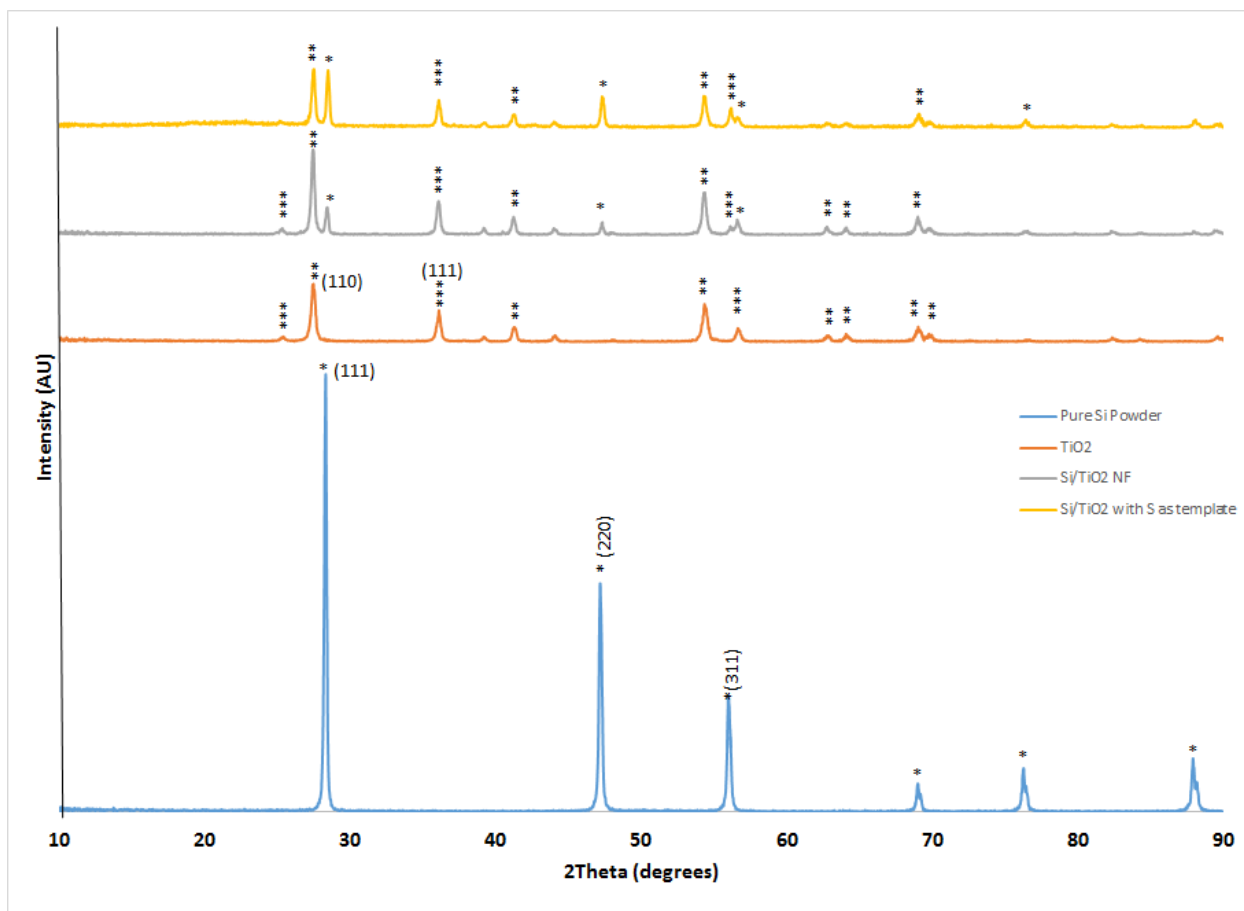


Figure 2: XRD patterns of noncarbonized Si micron-powder composite NFs (* cubic silicon, ** rutile titania, and *** anatase titania)

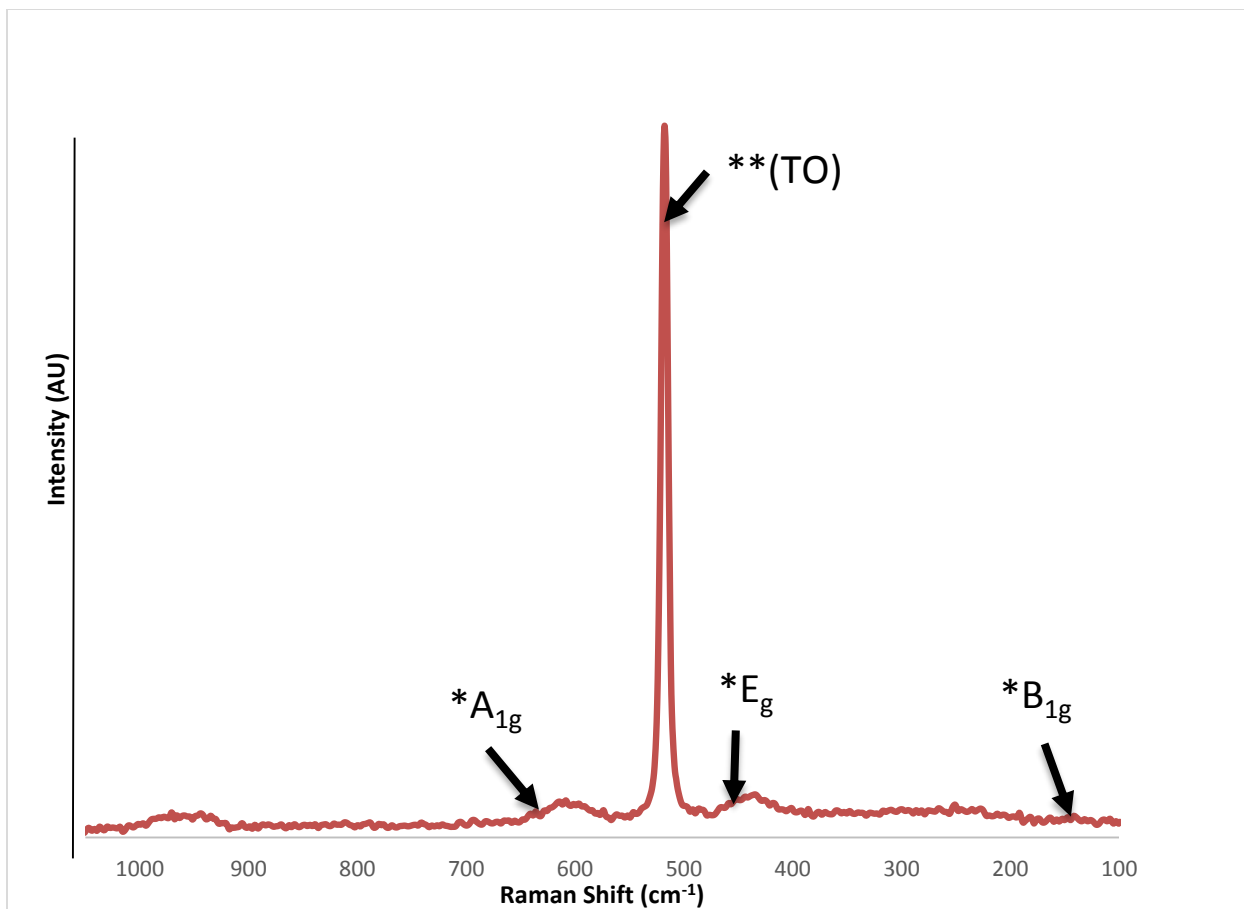


Figure 3: Raman spectrum of Si/TiO₂ with S as a template Note:*TiO₂, **Si

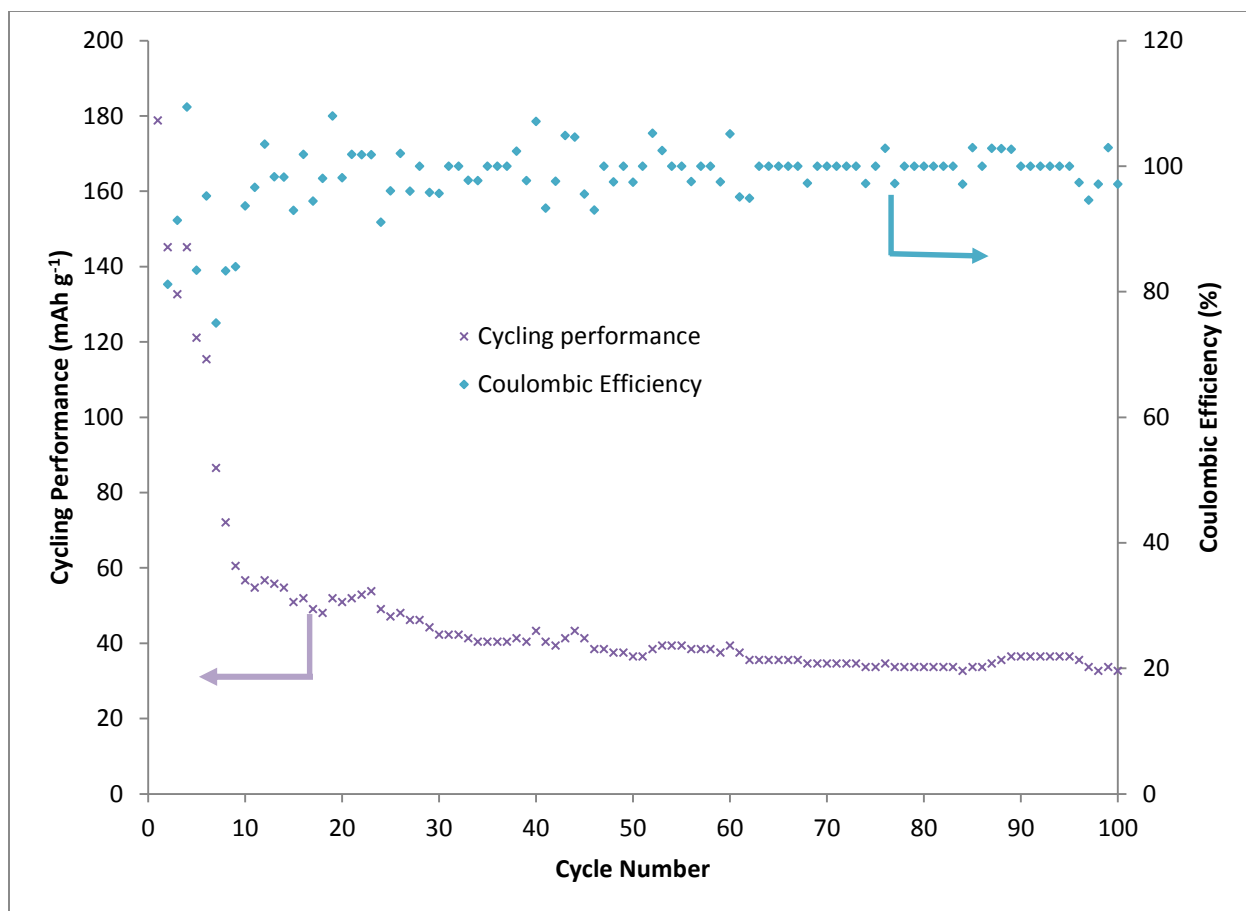


Figure 4: Cycling Performance and Coulombic Efficiency of Si/TiO₂ with S as a template